Sensor and Simulation Notes

Note 440

Fabrication and Testing of Two Collapsible Impulse Radiating Antennas

Leland H. Bowen and Everett G. Farr
Farr Research, Inc.

William D. Prather
Air Force Research Laboratory / Directed Energy Directorate

December 1999

Abstract

We continue here the development of the Multifunction Impulse Radiating Antenna (MIRA), which was introduced in Sensor and Simulation Note 413, and later refined in Sensor and Simulation Note 434. We describe here the design, fabrication and testing of two 1.22 m (48 in) diameter antennas that are collapsible, lightweight, and man-portable. Both antennas use conductive and resistive fabric on an umbrella frame. The first antenna is called a Collapsible IRA, or CIRA. The second antenna has a multifunction capability that was created with expansion seams in the reflector to allow the surface curvature (and beamwidth) to be adjustable. This antenna is called a Collapsible Multifunction IRA, or CMIRA. Both antennas were tested using standard time domain antenna range techniques, and the results were converted to IEEE standard gain in the frequency domain.

I. Introduction

We continue here our development of the Multifunction Impulse Radiating Antenna (MIRA) with a collapsible, compact, man-portable version. An earlier version of the MIRA was described in [1], and later refinements to the feed point were described in [2]. Reflector IRAs generally consist of a parabolic reflector with a TEM feed. Such a configuration results in very broadband performance (2 decades) with a very narrow beam. The first MIRA was motivated by the need for a broader beamwidth in certain special applications.

In this investigation, we develop antennas that not only have an adjustable beamwidth, but are also collapsible and man-portable. The design we selected resembles an umbrella, with a reflector and feed arms sewn from conducting and resistive fabric. We built two versions of the antenna that were similar, the difference being that one version did not have the multifunction capability. Therefore, the first version is called the Collapsible IRA, or CIRA. The second version had expansion seams in the reflector to allow the surface curvature to be adjustable. This antenna is called the Collapsible MIRA, or CMIRA.

The designs of both the CIRA and CMIRA were based on a 1.22 m (48 in) diameter parabolic dish with a focal length of 0.488 m (F/D = 0.4). For the CMIRA, the multifunction capability is implemented by flattening the dish by opening 4 expansion seams in the reflector surface. When the CMIRA is focused, the expansion seams are held closed with conducting Velcro.

The characteristics of the antennas were measured using time domain techniques. This was done both for the CIRA, and for the CMIRA in both focused and defocused modes. The time domain data was processed to obtain the normalized impulse response as described in [3]. Data was collected at 2.5° intervals in the H and E planes and converted to IEEE standard gain. The conversion from impulse response to IEEE standard gain is based on the derivation in Appendix A of [4] as modified in Section III of this report. The impulse response characteristics and the standard gain are presented. Plots of antenna gain vs. angle, at a constant frequency, are presented.

Several design successes and problems are discussed. The use of conductive fabric on an umbrella type frame provided a very good reflector that met the requirements for a man portable MIRA. We were very pleased with the TDR and impulse response of the CIRA. The main problems were caused by stretch in the fabric, high wind resistance, and difficulty in opening the antennas. Recommendations for addressing these issues are provided. A newer version of these antennas that address these concerns will follow in another note shortly.

II. Normalized Impulse Response

Before we get into the details of the antennas, we first review the parameters used to describe them. We have described antennas in the time domain with an impulse response, of the form $h_N(t)$. Here we provide a quick review.

In transmission mode, the antenna radiates a field on boresight, $E_{rad}(t)$, which is described by [3, eqn. 6.5]

$$\frac{E_{rad}(t)}{\sqrt{Z_o}} = \frac{1}{2\pi r c} h_N(t) \circ \frac{1}{\sqrt{Z_c}} \frac{dV_{src}(t)}{dt} \tag{2.1}$$

where Z_o is the impedance of free space, Z_c is the impedance of the 50 Ω feed cable, r is the distance out the observation point on boresight, $V_{src}(t)$ is the source voltage measured into a 50-ohm load, c is the speed of light in free space, and the " ∘ " symbol indicates convolution. In reception mode the antenna is described by [3, eqn. 7.5]

$$\frac{V_{rec}(t)}{\sqrt{Z_c}} = h_N(t) \circ \frac{E_{inc}(t)}{\sqrt{Z_o}} \tag{2.2}$$

where $E_{inc}(t)$ is the incident electric field on boresight. Note that the normalized impulse response, $h_N(t)$, completely describes the behavior of antennas with TEM feeds in both transmission and reception. If we have both a transmitting and receiving antenna, we can relate the received voltage to the source voltage by combining the above two equations as [3, eqn. 8.1]

$$V_{rec}(t) = \frac{1}{2\pi rc} h_{N,RX}(t) \circ h_{N,TX}(t) \circ \frac{dV_{src}(t)}{dt} \tag{2.3}$$

where $h_{N,RX}(t)$, is the normalized impulse response of the receive antenna and $h_{N,TX}(t)$ is the response of the transmit antenna.

To calibrate our measurement system, we use two identical TEM sensors. In this case, the antenna equation becomes

$$V_{rec}(t) = \frac{1}{2\pi rc} h_{N,tem}(t) \circ h_{N,tem}(t) \circ \frac{dV_{src}(t)}{dt} \tag{2.4}$$

which is very similar to equation (4.1) in [1]. The normalized impulse response of the sensors can be extracted from (2.4) as [3, eqn. 8.2]

$$\tilde{h}_{N,tem}(\omega) = \sqrt{\frac{2\pi rc \tilde{V}_{rec}(\omega)}{j\omega \tilde{V}_{src}(\omega)}} \tag{2.5}$$

The details of this sensor calibration are included in Section III of this report. Once a calibration has been performed with two identical antennas, then we can measure the response of an antenna under test by replacing one of the sensors with the antenna under test. The impulse response of the antenna then becomes

$$\tilde{h}_{N,AUT}(\omega) = \frac{2\pi r c \tilde{V}_{rec}(\omega)}{j\omega \tilde{V}_{src}(\omega)\, h_{N,tem}(\omega)} \tag{2.6}$$

and the time domain normalize impulse response is found with an inverse Fourier transform.

As a check on the reasonableness of our measurement, we normally calculate an aperture height, h_a, which can be related to the physical parameters of the antenna under test. To find the aperture height it is necessary to convert the normalized impulse response to the conventional impulse response. This conversion is given by [3, eqn. 7.4]

$$h_{N,RX}(t) = \frac{\tau_{p,RX}}{\sqrt{f_{g,RX}}}\, h_{RX}(t) \tag{2.7}$$

where $\tau_{p,RX}$ is defined as

$$\tau_{p,RX} = \frac{2\sqrt{Z_c\, Z_{a,RX}}}{Z_c + Z_{a,RX}} \tag{2.8}$$

and $f_{g,RX}$ is defined as

$$f_{g,RX} = \frac{Z_{a,RX}}{Z_o} \tag{2.9}$$

Here, Z_c is the cable impedance (50 Ω), Z_a is the antenna impedance, and Z_o is the impedance of free space (376.727 Ω). Since all of our measurements have the Antenna Under Test (AUT) as the receiver, only the "RX" versions of the equations are included here. For the 100 Ω TEM horn sensor used to make the antenna measurements, $\tau_{p,RX} = 0.942$ and $f_{g,RX} = 100/Z_o = 0.265$. For the CIRA and CMIRA, which have splitters in the feed circuit, we have $\tau_{p,RX} \approx 1$ from section VII of [3] and Z_a = 200 Ω for one feed arm so $f_{g,RX} = 200/Z_o = 0.531$. The integral of the conventional impulse response will be used later to determine the aperture height for both the sensor and the CIRA. The aperture height, h_a, corresponds to the jump in the integral

$$h_{a,RX} = \int_{\text{Impulse}} h_{RX}(t)dt \tag{2.10}$$

The aperture height is useful since the effective height (at midband) relates the incident electric field to the voltage into a scope by a simple proportionality [3, eqn. 3.4]

$$V_{rec}(t) \approx h_{eff}\, E_{inc}(t) \tag{2.11}$$

where

$$h_{eff} = \tau_{RX}\, h_{a,RX} \tag{2.12}$$

and

$$\tau_{RX} = \frac{2\, Z_c}{Z_c + Z_{a,RX}} \tag{2.13}$$

For the 100 Ω TEM horn, $\tau_{RX} = 0.667$ and for the CIRA and CMIRA $\tau_{RX} = 0.50$.

III. IEEE Standard Gain

It is frequently desirable to convert the impulse response developed in the previous section to IEEE standard gain. The IEEE standard gain is more widely accepted as a measure of antenna performance than the normalized impulse response. We provide here the derivation of the conversion process. This is modified somewhat from an earlier derivation in [4], which expressed the gain in terms of the conventional impulse response. Here we express the IEEE gain in terms of the normalized impulse response, $h_N(t)$.

We begin with the standard expressions in the frequency domain. Thus, the received power is

$$P_{rec} = A_{eff}\, S_{inc} \tag{3.1}$$

where S_{inc} is the incident power density in Watts/m^2 and A_{eff} is the effective aperture. Gain is related to effective aperture by

$$A_{eff} = \frac{\lambda^2}{4\pi} G \tag{3.2}$$

Combining the above two equations, we have

$$P_{rec} = \frac{\lambda^2 G}{4\pi} S_{inc} \tag{3.3}$$

Take the square root, and recast into voltages, to find

$$\frac{V_{rec}(\omega)}{\sqrt{Z_c}} = \frac{\lambda\sqrt{G(\omega)}}{2\sqrt{\pi}} \frac{E_{inc}(\omega)}{\sqrt{Z_o}} \tag{3.4}$$

where Z_c is the cable impedance, generally 50 Ω, and Z_o is the impedance of free space, 377 Ω.

Let us now compare the above equation to the standard equation for reception. Thus, we convert (2.2) of this paper into the frequency domain, obtaining

$$\frac{V_{rec}(\omega)}{\sqrt{Z_c}} = h_N(\omega) \frac{E_{inc}(\omega)}{\sqrt{Z_o}} \tag{3.5}$$

where $h_N(\omega)$ is the normalized antenna impulse response expressed in the frequency domain. The normalized impulse response, $h_N(t)$, is already known. To convert it to gain, we combine equations (3.4) and (3.5),

$$\boxed{G(\omega) = \frac{4\pi}{\lambda^2} |h_N(\omega)|^2 = \frac{4\pi f^2}{c^2} |h_N(\omega)|^2} \tag{3.6}$$

This formula allows us to convert our time domain impulse response to IEEE gain, so we will be consistent with others in the field.

IV. Data Acquisition System and Sensor Calibration

Next, we consider the data acquisition system and sensor calibration. The antenna measurement configuration is shown in Figure 4.1. It includes a Picosecond Pulse Labs (PSPL) 4015C Step Generator, which drives a TEM sensor. On the receive end, the AUT receives the signal, which is sampled by the SD24 sampling head and stored by the Tektronix 11801B Digital Sampling Oscilloscope (DSO). Data is then downloaded to a computer for processing by way of a GPIB connection. The output of the PSPL 4015C is a 4 volt step with a risetime of less than 30 ps as shown in Figure 4.5 of [1].

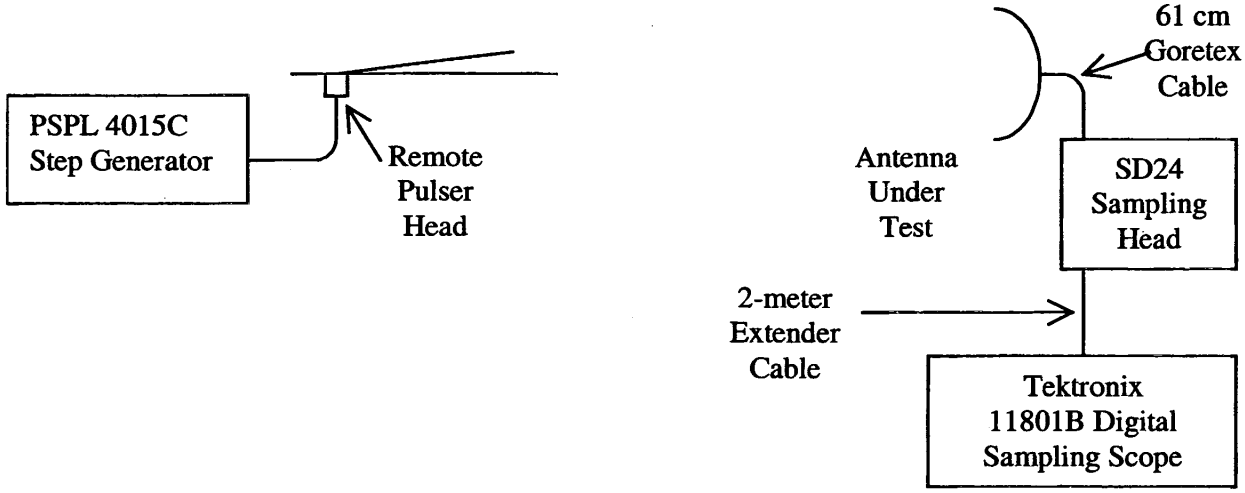

Figure 4.1 Experimental test setup

For the measurements performed here, a FRI-TEM-02-100 sensor was used. Farr Research manufactures four TEM sensors with the characteristics shown in Table 4.1. The FRI-TEM-02-100 was selected for use with the CIRA and CMIRA since they are required to operate over the range between 80 MHz and 2 GHz. The larger antenna provides a greater clear time and lower frequency response. We normally use the 100 Ω version of the sensors due to their greater sensitivity or h_{eff}.

Table 4.1

Model Number	Ground plane mm	Impedance Ω	h_{eff}** mm	3 dB point GHz	Clear Time ns
FRI-TEM-01-50	254 x 610	50	17	12	2
FRI-TEM-01-100	254 x 610	100	21	10	2
FRI-TEM-02-50	508 x 1220	50	30	7*	4
FRI-TEM-02-100	508 x 1220	100	42	6	4

* Estimated

** $V_{out}(t) \approx h_{eff} \times E_{inc}(t)$.

A picture of an FRI-TEM-02-100 sensor is shown in Figure 4.3. The TDR of the sensor is shown in Figure 4.4. In order to calibrate the sensor, the AUT in Figure 4.1 was replaced with a second FRI-TEM-02-100 sensor. The calibration was performed with the sensor apertures 20 m apart and 2.1 m above the ground. This provides 1.5 ns delay before the ground bounce signal arrives.

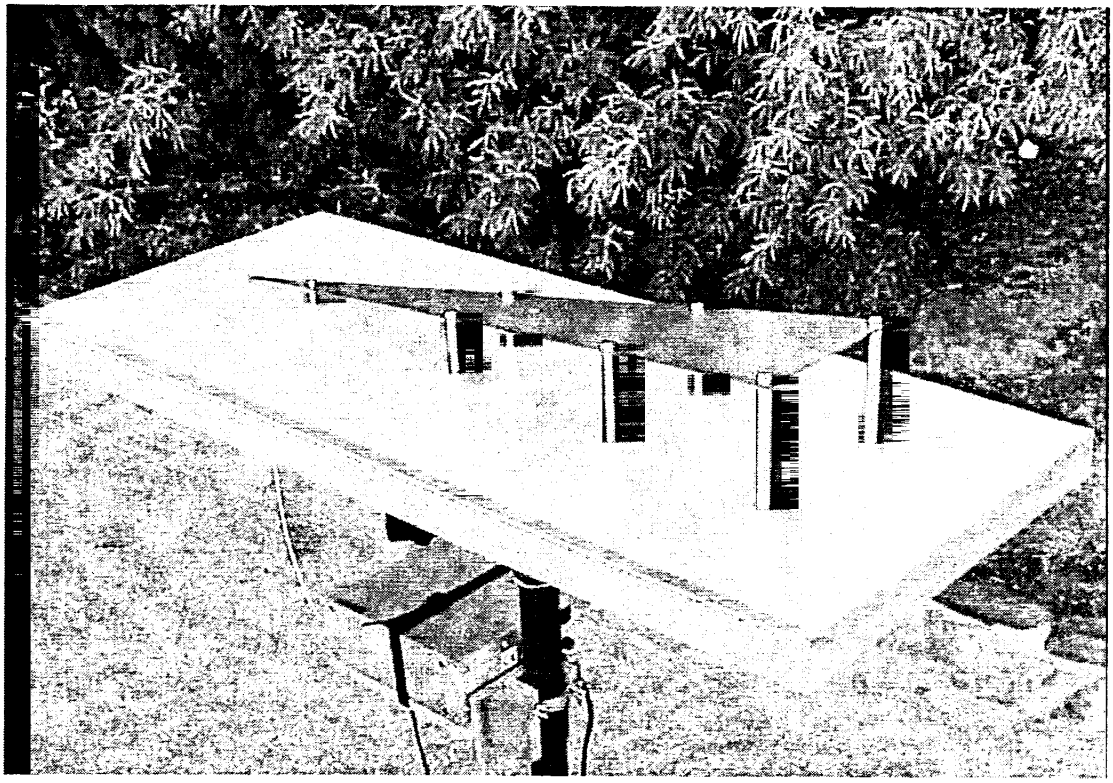

Figure 4.2 FRI-TEM-02-100 on tripod with PSPL 4015C pulser.

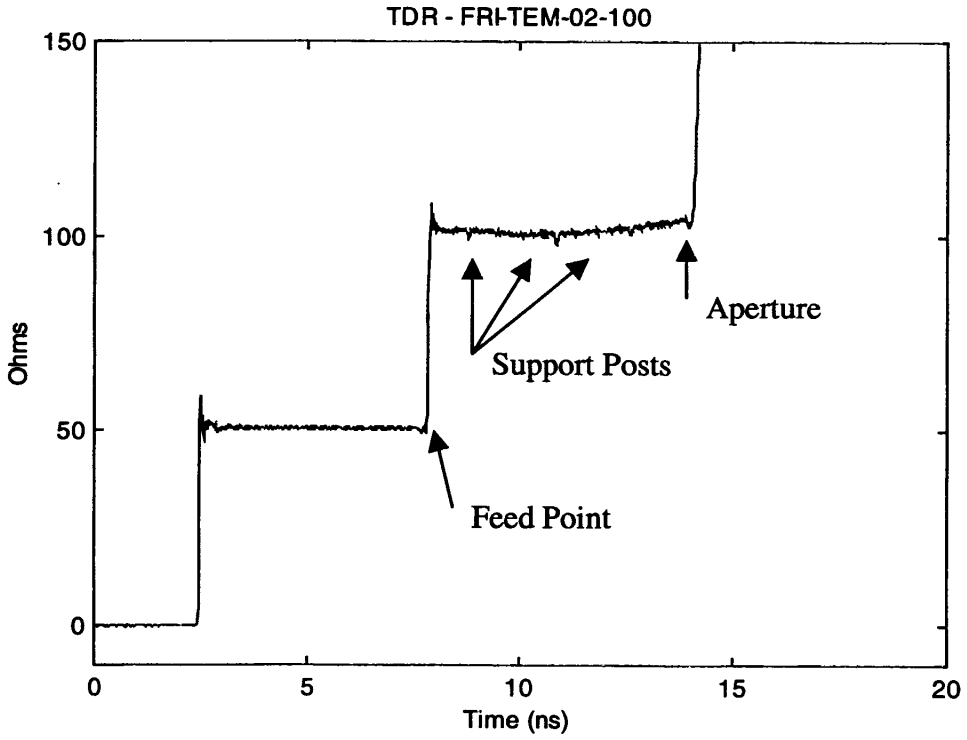

Figure 4.3 TDR of an early prototype of the FRI-TEM-02-100 sensor used in this note.

The sensor calibration is detailed in Figures 4.4 – 4.8. The voltage measured at the receiving sensor was truncated shortly after the impulse signal to remove the ground bounce. Also, the signal was zero padded out to 20 ns for processing to improve the low frequency response. These modifications are shown in Figure 4.4. The frequency response is extremely flat as shown in Figure 4.6. The jump in the integral of the conventional impulse response shown in Figure 4.8 gives a value for h_a of 62.5 mm. The aperture height is 125 mm which gives a theoretical value for h_a of 62.5 mm [3]. Therefore, the measured value is equal to the expected value. The effective height at midband, $h_{eff} = h_a \times \tau_{RX} = 40$ mm, since $\tau_{RX} = 0.667$.

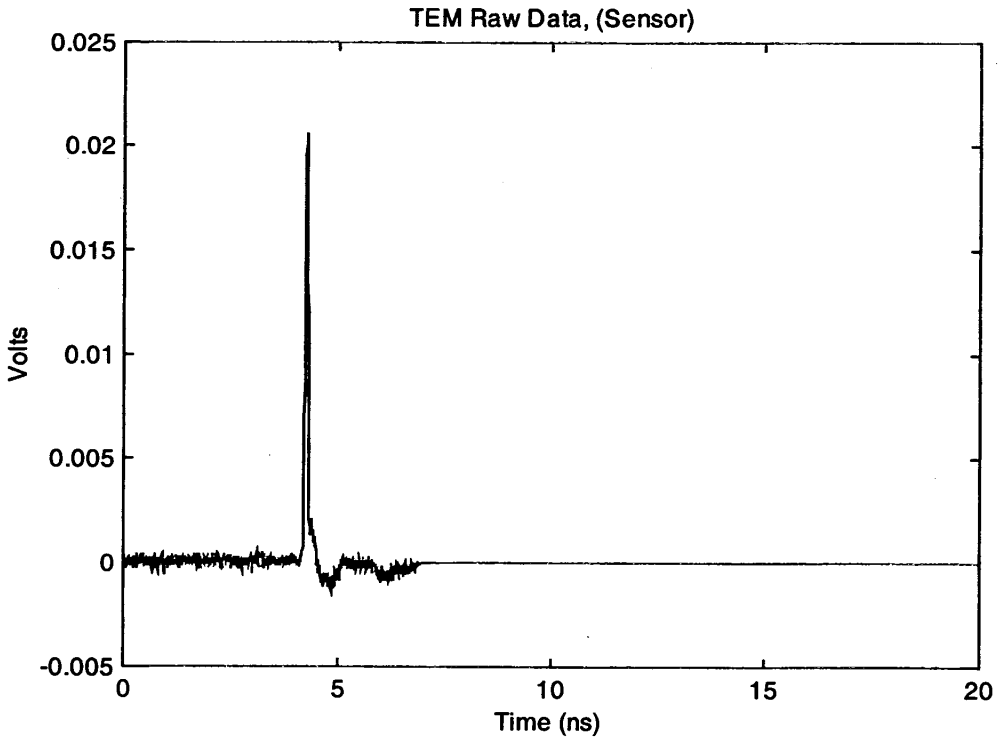

Figure 4.4 FRI-TEM-02-100 Data with ground bounce removed and zero-padded

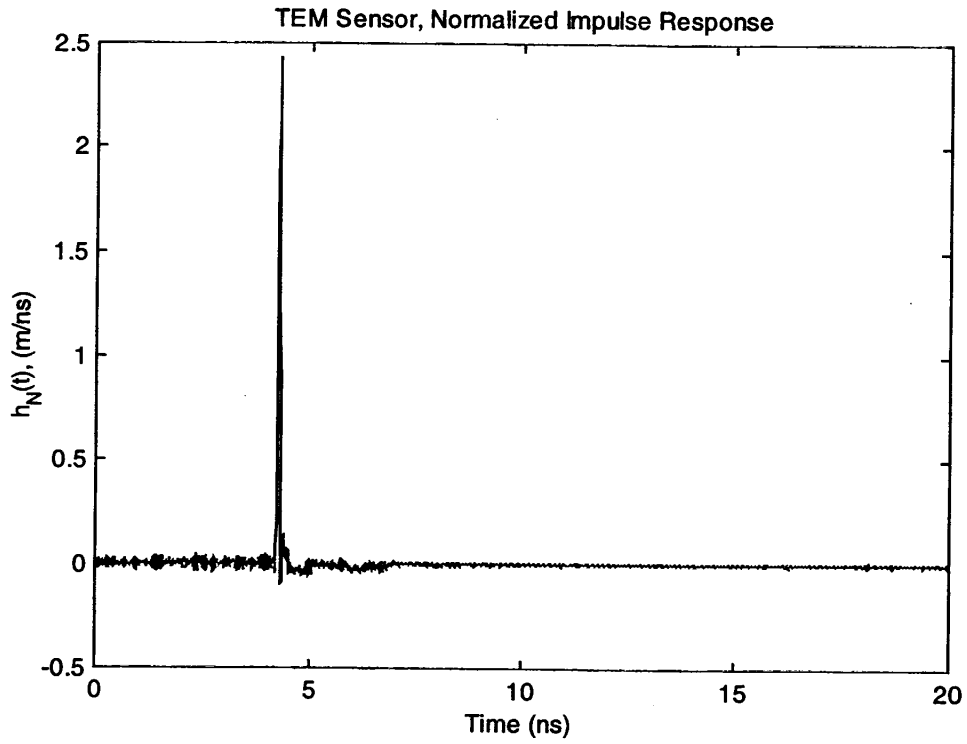

Figure 4.5 Normalized Impulse Response [3] (FWHM = 52 ps)

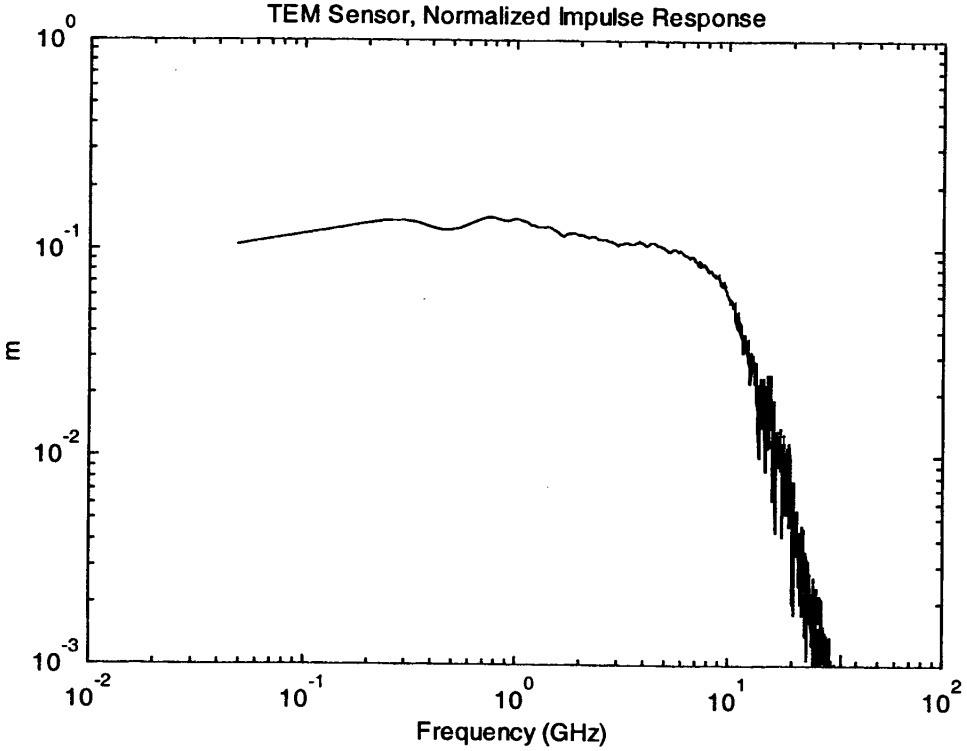

Figure 4.6 Normalized Impulse Response in Frequency Domain

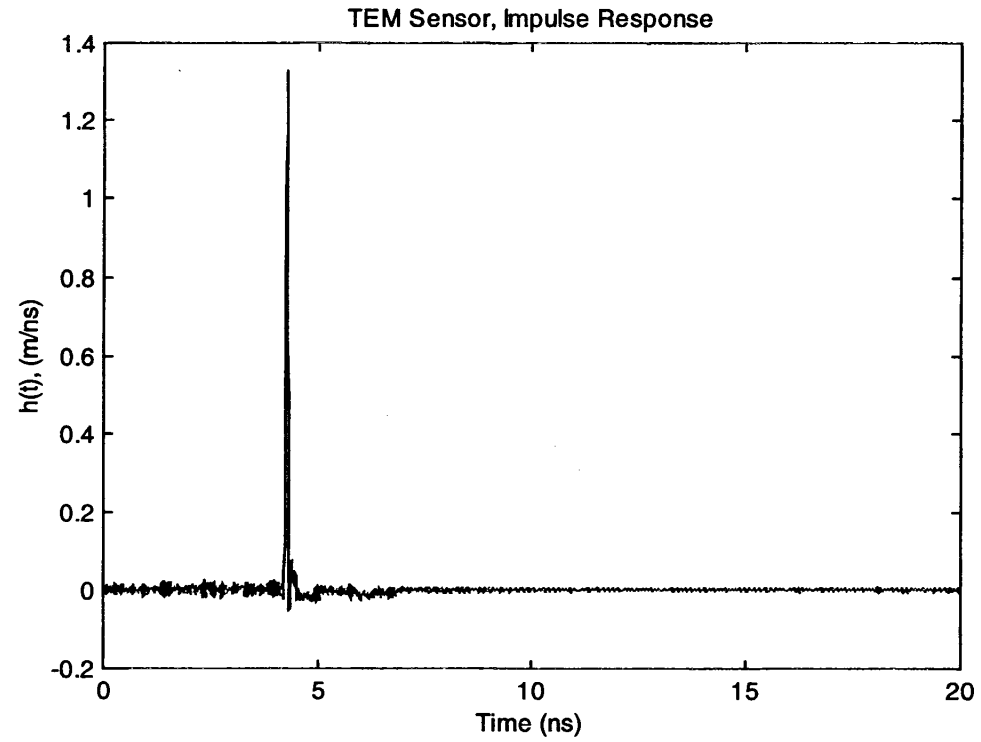

Figure 4.7 Conventional Impulse Response [3]

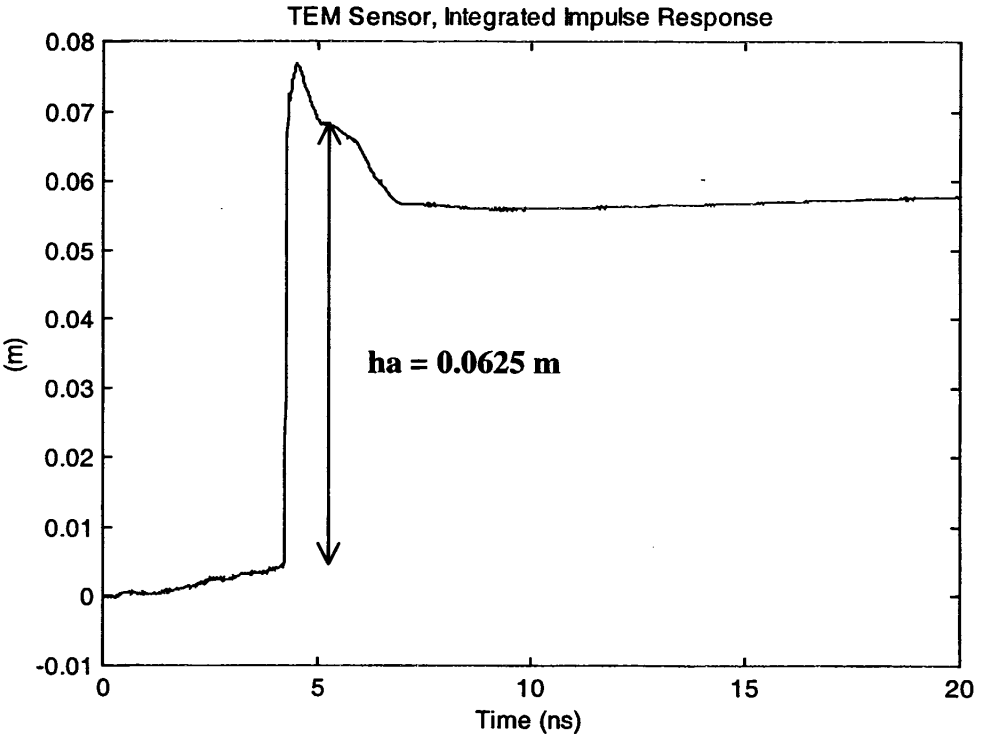

Figure 4.8 Integral of Impulse Response (ha = 0.0625 m)

V. CIRA Design and Fabrication

We provide here now the details of the CIRA design and fabrication. The collapsible antennas are designed to open and close like an umbrella. The reflectors are 1.22 m (48 in.) in diameter with F/D = 0.4. The reflectors are sewn from conductive fabric. The feed arms are made from a combination of conductive and resistive fabrics. The feed point was reinforced for mechanical strength. The splitter was provided by Prodyne Technologies. It consisted of a 50 Ω input impedance connector, which then split into two 95 Ω cables.

We found it necessary to build two versions of the umbrella. One version has four seams in the reflector to allow the surface curvature of the reflector to be adjustable. This is the feature that allows one to have an adjustable beamwidth. The other version of the umbrella has a fixed (focused) reflector, with no adjustments possible. It was necessary to build one of each, in order to understand the effect of the four seams in the reflector surface. Thus, we are interested in whether the four seams have any effect in the antenna pattern, when compared to a comparable design without the seams.

The mechanical design of the collapsible antennas is shown in Figure 5.1. For simplicity, this figure includes only a cross-sectional view of half of the antenna in the open position. The cross-sectional view is taken through one of the four feed arms. The antenna is supported by a tripod adapter connected to the back (bottom in Figure 5.1) of the can. This can contains the splitter and helps support the lower yoke and the center rod or tube. The upper yoke slides onto the center rod as indicated by the double-ended arrow. In the open position a nylon nut attached to the upper yoke engages threads on the center rod to hold the yoke in the lower position. This provides the required force, through the push rods, to hold the stays in place.

The reflector is made up of 20 panels of conductive rip-stop nylon as shown in Figure 5.2. In theory, the variation of the surface from a true paraboloid should be about 7.6 mm for the for this size reflector. This is only about 5% of the wavelength at the highest frequency of interest (2 GHz). The actual deviation from the ideal was somewhat greater than this due to stretch and wrinkles in the fabric and slight inaccuracies in the sewing. The depth of the dish was approximately 165 mm rather than 190 mm as desired.

Next, we consider the construction materials and their characteristics. The can, lower yoke and center tube are all made of aluminum to reduce weight. The upper yoke is nylon for strength and to reduce shadowing. The stays and push rods are made of a fiberglass reinforced material, which was so stiff that it normally required two people to open the antenna. (This will be fixed in the next version.) The dielectric parts at the feed point were all UHMW (Ultra High Molecular Weight Polyethylene), which provides a nice combination of strength and low dielectric constant. The reflector was made of copper and nickel plated rip-stop nylon. This material is strong and lightweight and has an electrical surface resistivity of less than 0.1 Ω/square. The fabric resistors were constructed from a polypyrrole treated woven polyester with a surface resistivity in the range of 200 Ω/square.

When closed, the antennas are slightly over 127 mm (5 in.) in diameter and 737 mm (29 in.) long. The antennas weigh approximately 2.8 kg (6 lb.). While this size and weight are acceptable, we hope to reduce the diameter and weight for future versions.

The design and construction of the feed point presented us with several challenges, based on the requirements for both mechanical rigidity and electrical performance. Based on lessons learned while modifying the first MIRA [2], a reasonably strong feed point was developed, that met our electrical requirements. The design included a dielectric UHMW cross to support the copper tips attached to the fabric feed arms. Careful attachment of the two coax cables from the splitter resulted in a very flat TDR as shown in the next section. A protective cover was designed for the CMIRA feed point. The cover was made of UHMW and it seemed to have little effect on the TDR. Photographs of the feed point are included in Section VII.

Although the basic design was very successful, several problems were encountered. One problem was the high wind resistance of the 1.22 m diameter rip-stop nylon dish. The antennas were strong and held their shape well in the wind. However, during one afternoon of testing, both antennas were blown over and damaged by rather modest gusts. The feed point on the CIRA was damaged and the center rods on both antennas were bent. Both antennas were repaired and a protective cover was added to the CIRA feed point. Later versions of this antenna will address the issues of wind loading and mechanical strength.

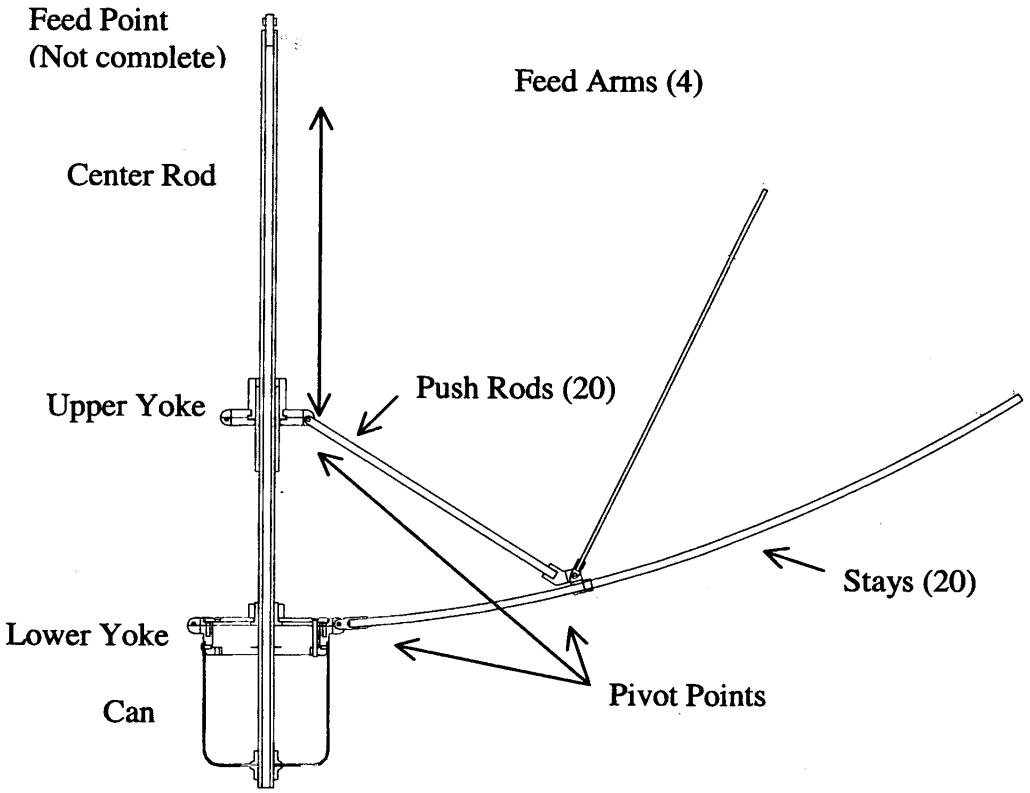

Figure 5.1 CIRA umbrella design

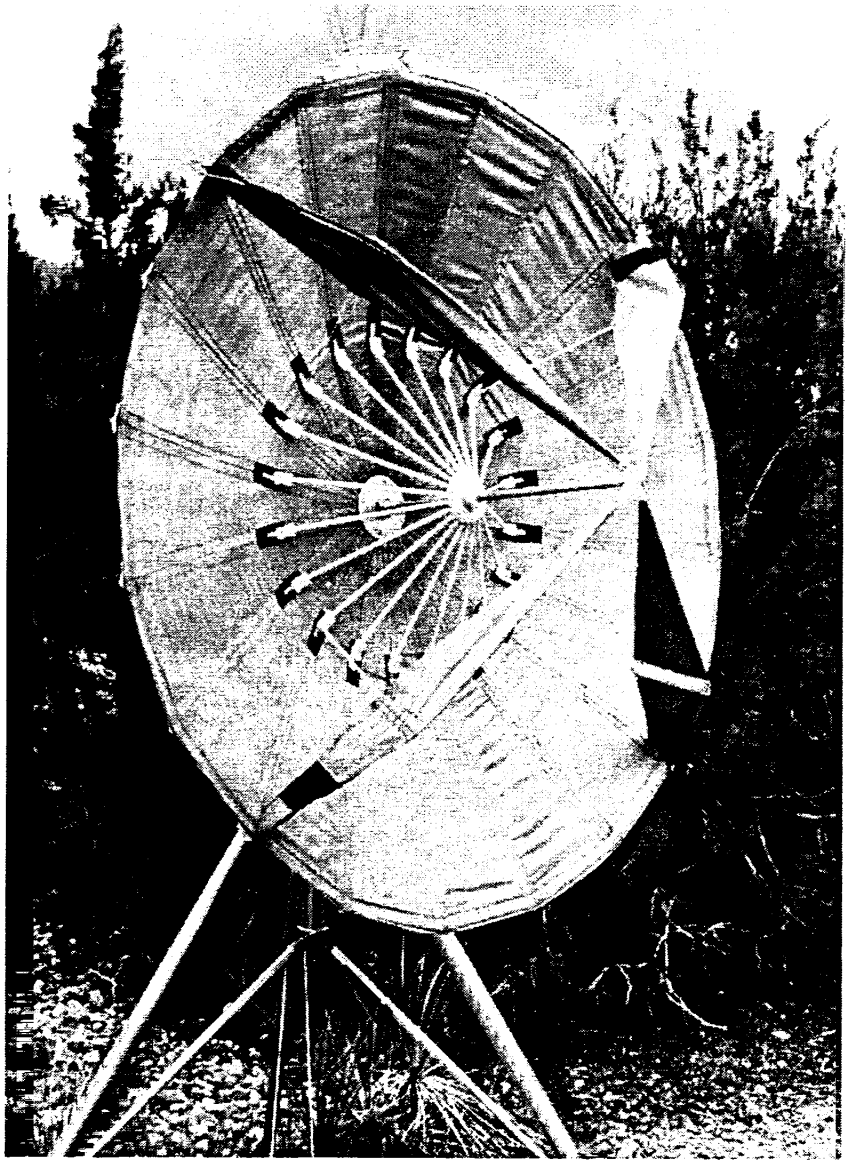

Figure 5.2 CIRA mounted on tripod for testing

VI. CIRA Data

The characteristics of the CIRA were measured using a PSPL 4015C Step Generator driving a TEM horn antenna as described in Section IV. The Step Generator has a 4 V output with a 25 ps risetime. The TEM horn was a prototype of the FRI-TEM-02-100 sensor produced by Farr Research. The response of the CIRA was recorded using a Tektronix 11801B Digital Sampling Oscilloscope. The distance between the antennas was 20 m and the height was 3 m. Antenna patterns in the H- and E-planes were made at 2.5° increments. The data are zero-padded out to 20 ns to provide information on the frequency response down to 50 MHz. Also, the IEEE standard gain is computed and plotted on boresight as a function of frequency and at various frequencies as a function of angle off boresight.

The observed data are as follows. The TDR of the CIRA is shown in Figure 6.1. We were very pleased with the flatness of the TDR, especially at late time. The section marked "Feed Cable" is actually two 95 Ω coaxial cables in parallel. In Figures 6.2 – 6.7, we provide the boresight characteristics of the CIRA. The FWHM of the normalized impulse response is 100 ps. Figure 6.5 is the IEEE gain as a function of frequency on boresight. The antenna is usable from below 50 MHz to above 8 GHz. The midband effective height of the antenna (defined earlier in (2.11)) is found from the integral of the impulse response shown in Figure 6.7 to be 0.31 m. This is 78 % of the theoretical value of 0.396 m based on formulas in [3, 5].

Next, we provide the IEEE gain as a function of angle in Figures 6.8 and 6.9, for frequencies from 100 MHz to 4 GHz. The antenna pattern in the H plane, based on the peaks of the raw voltage measurements, is shown in Figure 6.10. The raw data at several angles in the H plane are shown in Figure 6.11. Figures 6.12 and 6.13 contain similar data for the E plane. The half voltage beamwidth is 13° in the H plane and 11° in the E plane. If we choose to use the half power beamwidth, we have 7° and 6° in the H and E planes respectively.

Based on this data, we now consider the beam width. In [1] the half field beamwidth (HFBW) was defined as the angle between the two locations in a pattern cut where the field is down by half from the peak. Since the measured (raw) voltage is proportional to the incident electric field (2.11), this is the same as the half voltage beamwidth used above. Using this definition and the calculation methods of [1], we can estimate the HFBW in the H plane to be 3° and in the E plane to be 4° for an ideal antenna. The theoretical fields at discrete angles of 0°, 1°, 2°, and 5° off boresight were used for the above estimates. The angles for the CIRA are 3.5 – 4.6 times these values. This is due largely to the antenna being somewhat out of focus as discussed elsewhere.

Note that there are some bumps in the boresight impulse response of the CIRA at low frequencies, as shown in Figure 6.4. We investigated whether these bumps could be reduced by eliminating the ground reflection. When we tried this, the low-frequency bumps in the resulting impulse response were indeed smoother, but they were not eliminated.

It appears that low-frequency measurements of this antenna are problematic below 400 MHz or so. The pattern cuts taken at 98 and 195 MHz (Figures 6.8 and 6.9) have a sharp drop at 15° that is not characteristic of low-frequency patterns. We expect low-frequency pattern cuts to

vary slowly. This behavior is seen in the pattern cuts at 391 MHz and higher. It is possible that the problems arise because the measurements were not taken in an anechoic chamber, however, measurements in a chamber are also known to have problems at low frequency. We will continue to explore methods of extending the low-frequency range of time domain antenna measurements.

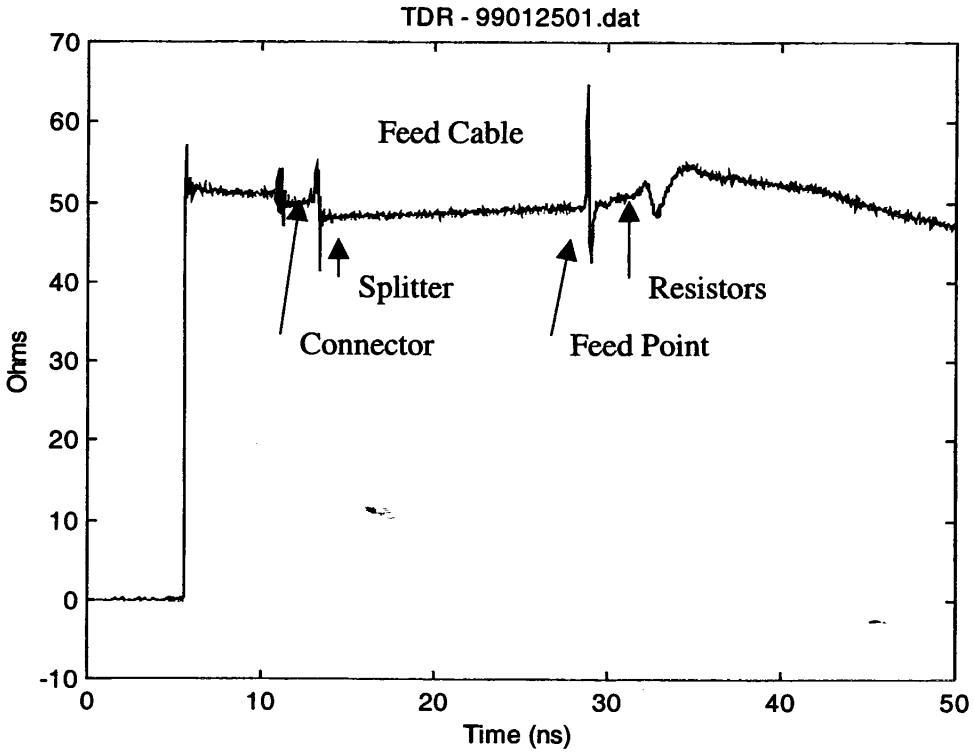

Figure 6.1 TDR of CIRA

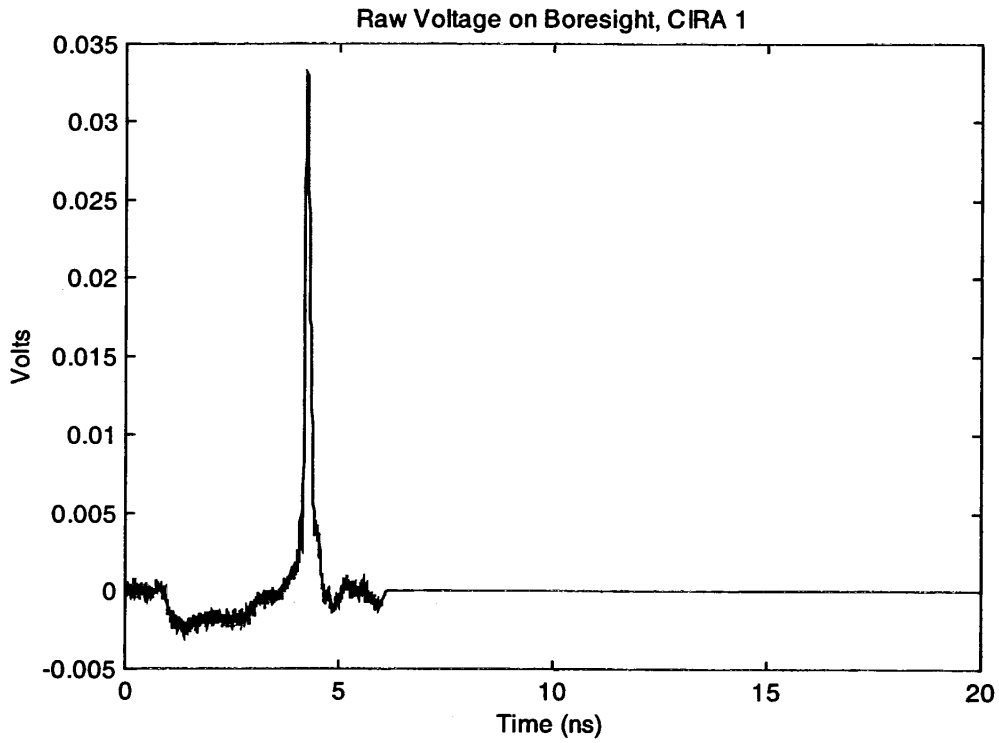

Figure 6.2 Raw Data on Boresight with Ground Bounce Removed and Zero-Padded

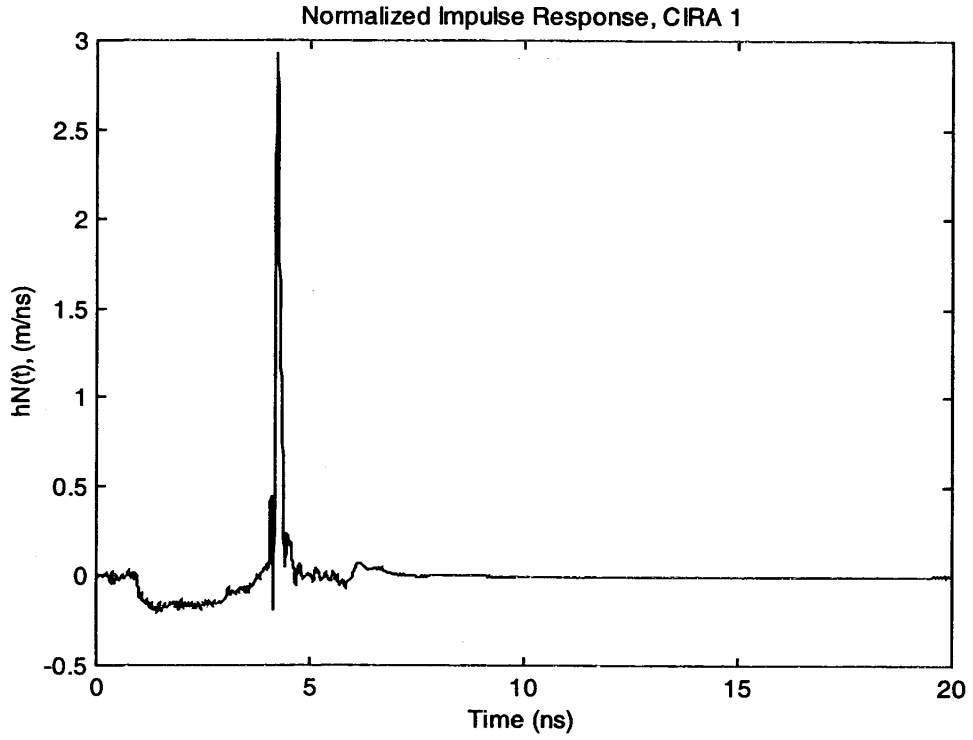

Figure 6.3 Normalized Impulse Response [3] (FWHM = 105 ps)

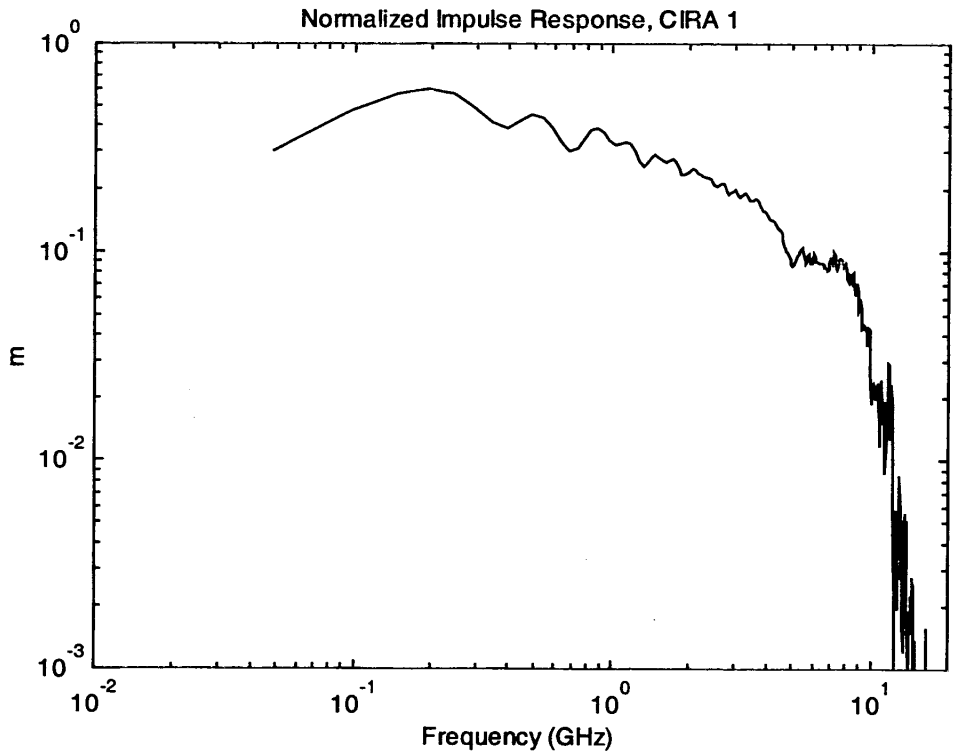

Figure 6.4 Normalized Impulse Response of the CIRA on Boresight.

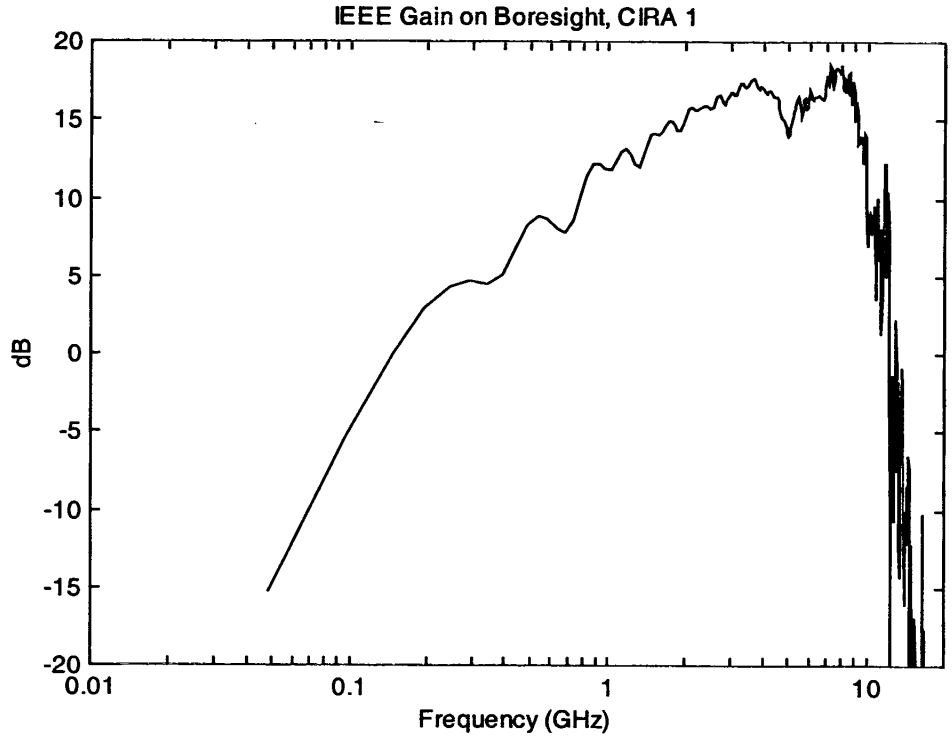

Figure 6.5 IEEE Gain of the CIRA on Boresight.

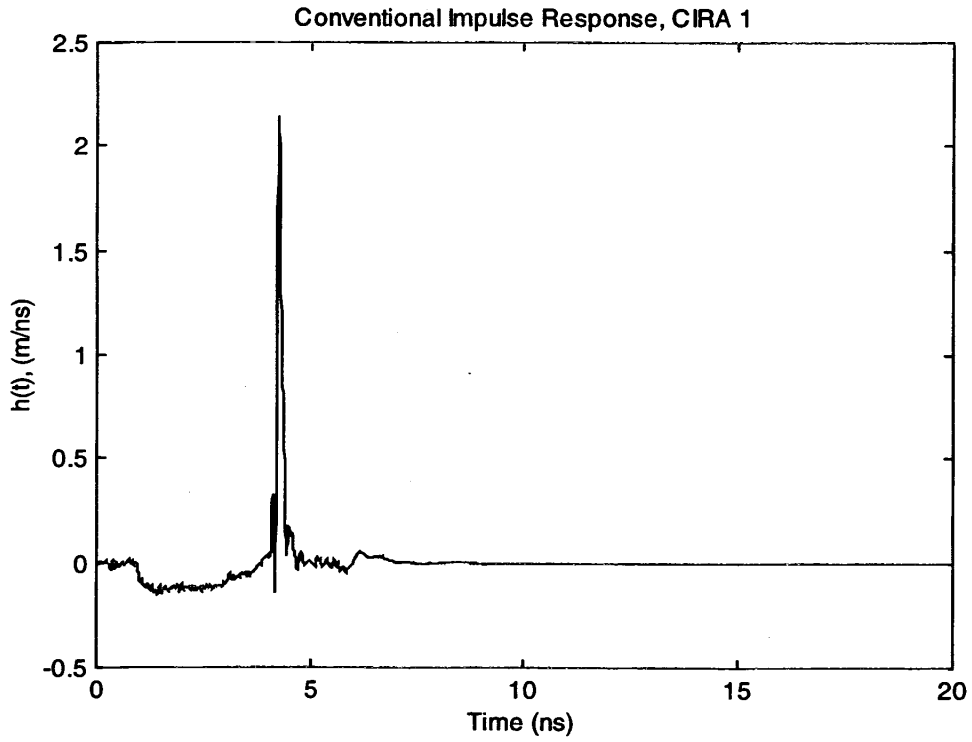

Figure 6.6 Conventional Impulse Response, $h(t)$ [2]

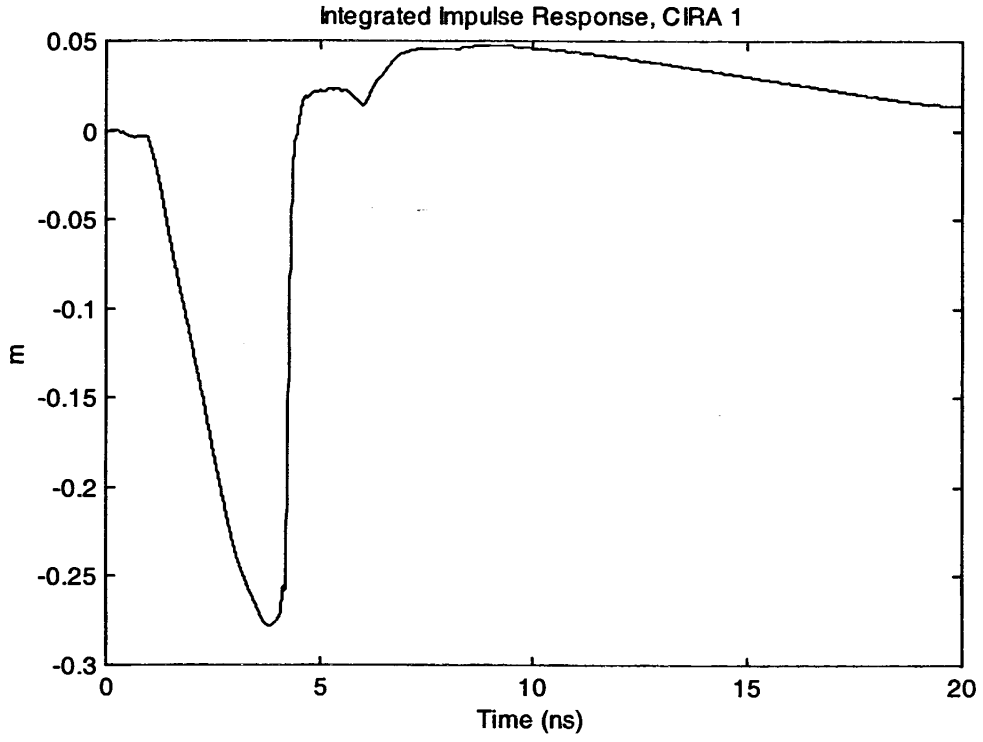

Figure 6.7 Integrated Impulse Response (h_a = 0.31 m)

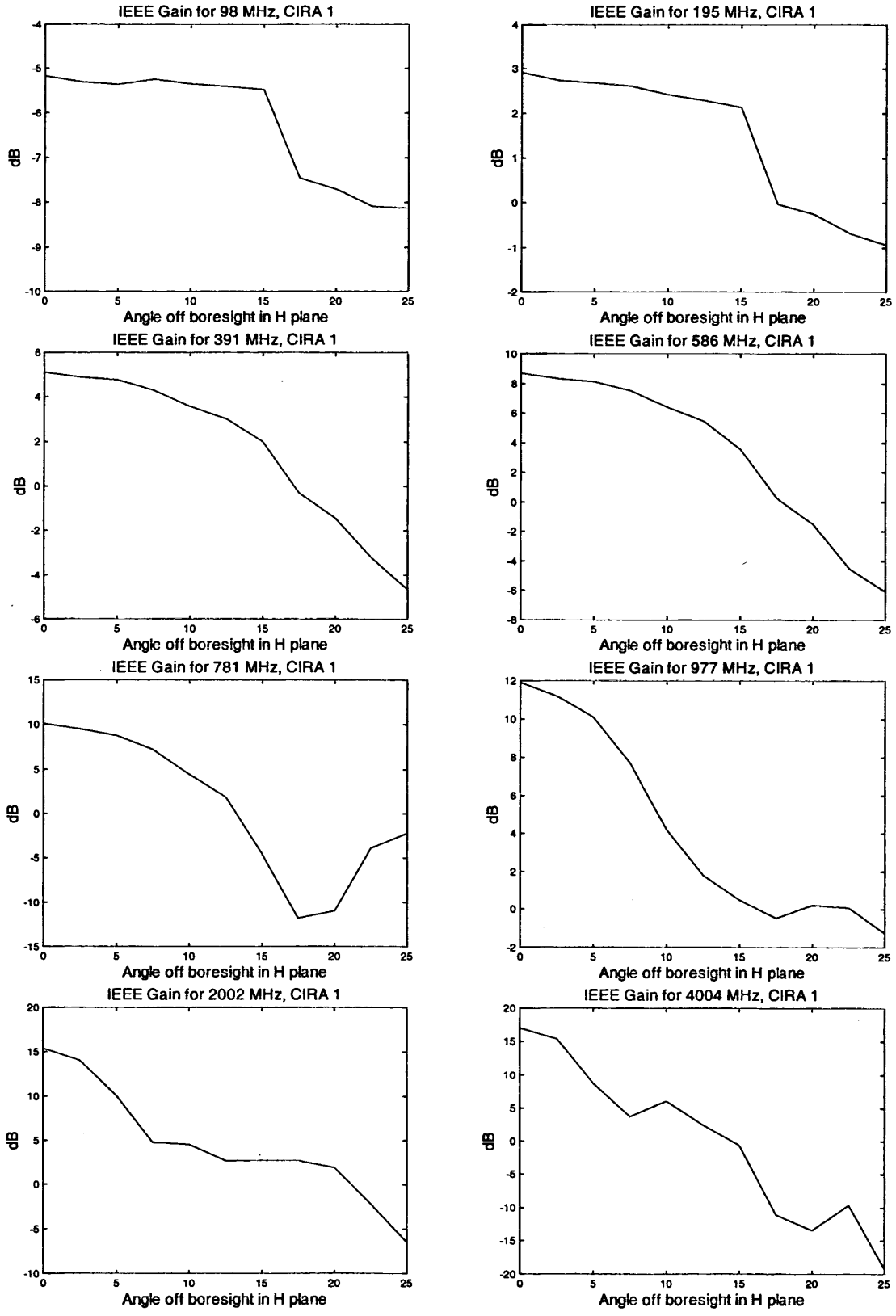

Figure 6.8 IEEE Gain vs. Angle off boresight in H plane

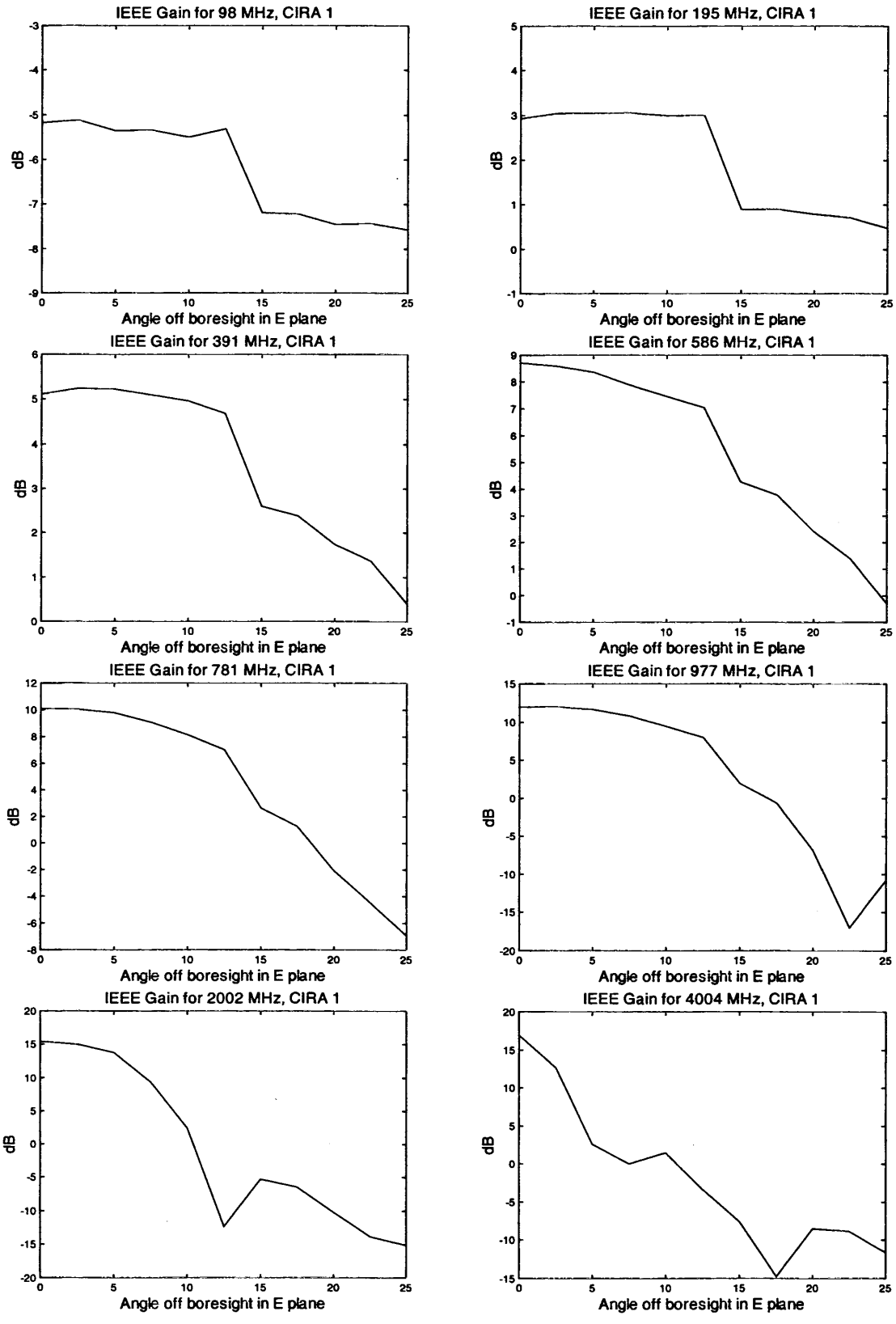

Figure 6.9 IEEE Gain vs. Angle off boresight in E plane

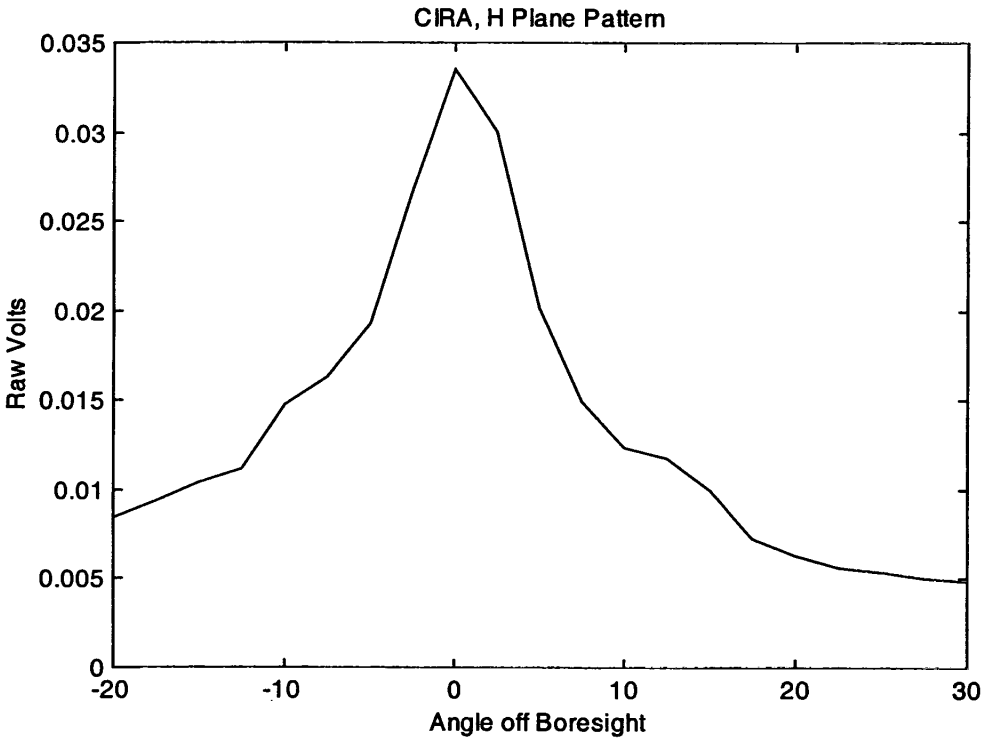

Figure 6.10 Antenna pattern based on raw voltage measurements in H plane.

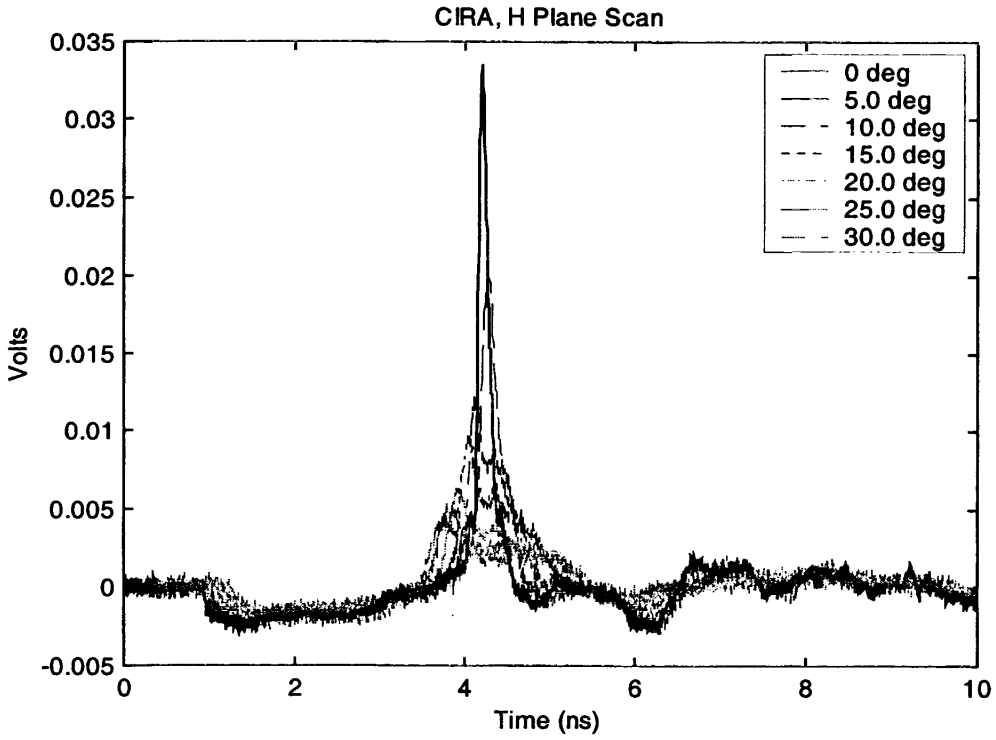

Figure 6.11 Raw voltage at several angles in H plane.

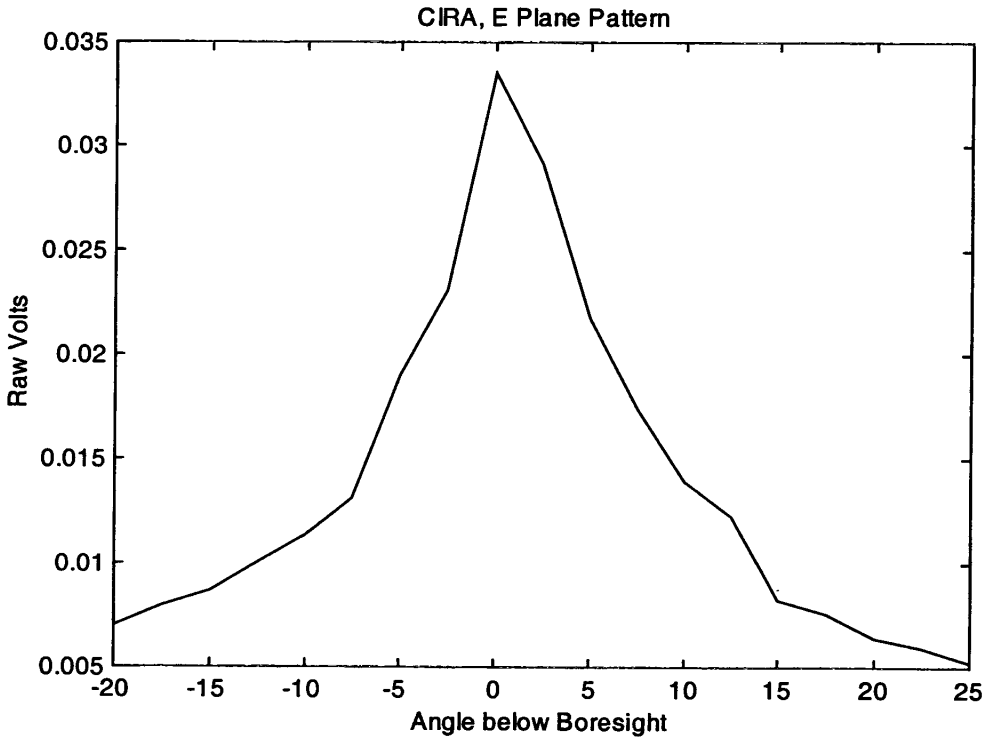

Figure 6.12 Antenna pattern based on raw voltage measurements in E plane.

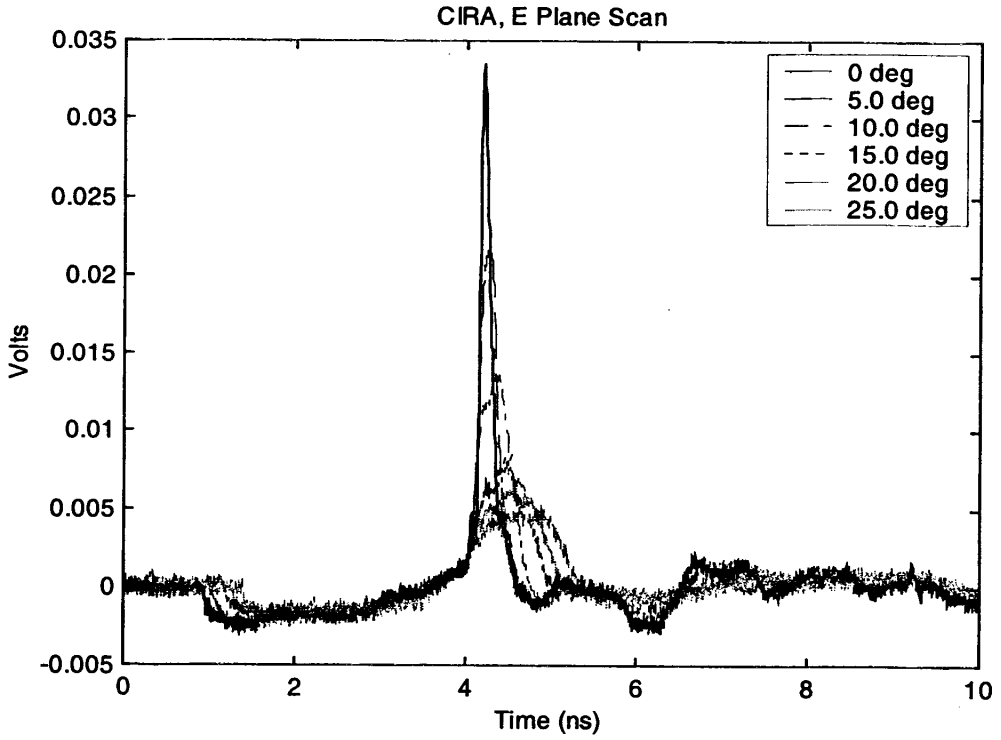

Figure 6.13 Voltage measurements at several angles in E plane.

VII. CMIRA Fabrication

The CMIRA is simply a CIRA with a multifunction capability added. This is implemented by inserting four expansion seams in the fabric reflector to flatten the reflector. In addition, extension sections must be added to the feed arms between the resistor section and the reflector. Having built such a device, we then must characterize it in two positions, focused and defocused.

As with the CIRA, this antenna, when in the focused mode, had a diameter of 1.22 m (48 in) and a focus of 0.488 m (19.2 in). This gives a ratio F/D of 0.40 as desired and a depth of 190 mm (7.5 in). In the defocused mode, the reflector is flattened somewhat, which increases the diameter to 1.284 m and the focus to 1.44 m. This gives a depth of 72 mm. Since the feed point does not move with respect to the reflector, we have from [1], $f_f = F_2/F = 0.488/1.44 = 0.34$.

As with the CIRA, the stretch in the fabric and slight variations in sewing the reflector panels caused some deviations from an ideal parabolic dish. In this case the depth of the CMIRA in focused mode was approximately 146 mm. Since the depth is given by $D^2/16\ F$ we can compute the new focus (F) to be 0.64 m. Therefore, at best we have $f_f = 0.77$.

The expansion seams in the reflector presented us with a particularly difficult challenge, since they need to be conductive when closed. We originally tried to coat a variety of zippers with a conductive layer. However, the experiment had never been tried before, and the coating did not stick. For that reason, we used conductive Velcro to form a conductive seal. Conductive Velcro is a standard item available off-the-shelf.

Various features of the CMIRA are shown in Figure 7.1. The first picture (top, left) shows the CMIRA in focused mode. The second picture shows the CMIRA in the open or defocused mode. The expansion seams can be seen in both pictures. In the defocused mode the CMIRA reflector is almost flat. In both modes the actual depth of the dish is less than desired due to stretch in the fabric. The third and forth pictures detail the feed point construction. A UHMW cover was added to the feed point of the CMIRA, as shown in the third picture, to protect the rather delicate wiring connections. In the forth picture the cover is removed to show the copper tips attached to the fabric feed arms and the location of the coax cable feeds. One feed passes through the center tube to the splitter in the can. The other feed coax follows one of the feed arms out to the rim of the reflector and then follows one of the stays to the splitter. The copper tips on the feed arms are required for strength and to provide a means to solder the coax cables to the feed arms in the required configuration. The fifth and sixth pictures show details of the Velcro closures in the feed arms and reflector of the CMIRA. In both pictures the Velcro extensions are in the closed or focused position. The resistor and one of the feed coax cables with a ferrite bead are shown in the fifth picture. The resistor is constructed of resistive fabric. The ferrite bead is required where the coax cable crosses the resistor.

As with the CIRA, we found the wind load on CIRA was too high, even under relatively mild wind conditions. To mitigate this problem, an open weave fabric with much higher strength and lower ability to stretch will be used in the next CIRA.

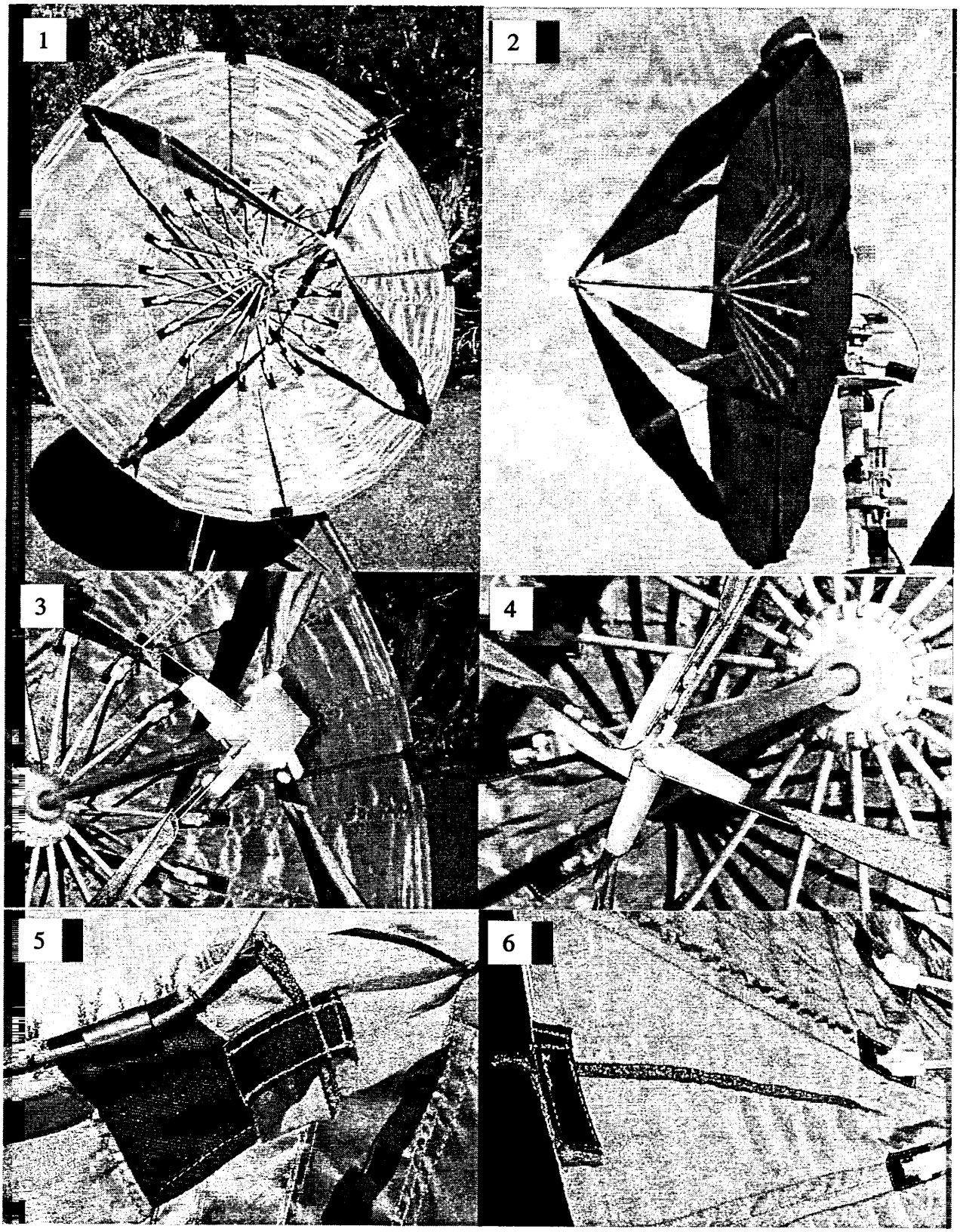

Figure 7.1 CMIRA. 1. Focused, 2. Defocused (during test), 3. Feed point with cover, 4. Feed without cover, 5. Resistor and Velcro seam, 6. Velcro seam in closed position

VIII. CMIRA Data

We present here the data for the CMIRA. The TDR of the CMIRA is shown in Figure 8.1. The data for the focused CMIRA are shown in Figures 8.2 – 8.13. In Figures 8.2 – 8.7 we provide the boresight characteristics of the CMIRA. Figure 8.5 is the IEEE gain vs. frequency. The antenna is usable from below 100 MHz to above 7.5 GHz in the focused mode. The gain of the CMIRA at higher frequencies is somewhat lower than the gain of the CIRA. Even in the focused mode the CMIRA is much flatter than it should have been. This was due to stretch in the rip stop nylon reflector and in the Velcro used to adjust the shape of the dish. We expect that the data from the CIRA are more typical of a focused CMIRA than the data presented here. The midband effective height of the antenna (defined earlier in (2.11)) is found from the integral of the impulse response shown in Figure 8.7 to be 0.26 m. We expect this height to be the same as the CIRA. The problem of the reduced height is discussed below.

Two antennas were built to study the effect of the conductive Velcro seams. As mentioned in the last section, the CMIRA in the focused mode was out of focus by approximately 44 mm. This is 19 mm more than the CIRA. For the CIRA we have $f_f = 0.87$ and for the CMIRA $f_f = 0.77$. (In a perfectly focused antenna, $f_f = 1$.) Therefore, the differences in the responses of the CIRA and CMIRA were primarily a result of the difference in reflector depths, not the presence of the expansion seams. Because of this, we were unable to isolate the effect of the expansion seams alone.

The IEEE gain in focused mode is provided as a function of angle in Figures 8.8 and 8.9 for frequencies from 50 MHz to 2 GHz. The antenna pattern in the H plane, based on the peaks of the raw voltage measurements, is shown in Figure 8.10. The raw data at several angles in the H plane are shown in Figure 8.11. Figures 8.12 and 8.13 contain similar data for the E plane. From the peak values at the various angles we can get the beamwidth in the major planes. The half voltage beamwidth is 24° in the H plane and 17° in the E Plane. The beamwidth for the CIRA was at least 6° narrower in both planes. For the half power case, we have beamwidths of 10° in the H plane and 11° in the E plane.

The data for the CMIRA in defocused mode is provided in Figures 8.14 – 8.25. The IEEE gain as a function of frequency is shown in Figure 8.17. From this figure we observe that the defocused CMIRA has a low-end 3 dB frequency of around 100 MHz and a high-end 3 dB frequency of around 1 GHz. The midband effective height of the antenna (as defined in (2.11)) is found from the integral of the impulse response in Figure 8.19 to be 0.21 m. This result is a little surprising to us, since our intuition is that the midband effective height for the defocused configuration should be the same as that for the focused configuration, or 0.32 m.

As a check on the discrepancy between the h_a's of the CIRA and CMIRA, we were able to do a similar comparison between an 18-inch (0.46 meter) diameter focused IRA and a flat version of the same antenna, called a Pulse Radiating Antenna Element, or PRAE. The focused IRA has a focal length of 0.23 m (F/D = 0.5). The PRAE has the feed point located 0.23 m from a flat plate reflector. For the IRA, h_a = 125 mm and for the PRAE, h_a = 105 mm. This variation is much less than that for the CIRA but is still not as close as expected. The theoretical value of

h_a for this antenna is 149 mm from [2, 5]. We can also compare these results to the aperture height, h_a, of the modified 18-inch diameter MIRA which is described in [2]. This device, when focused, closely resembles the 18-inch diameter IRA, and has h_a = 100 mm [2]. This value is smaller than expected and in some ways only adds to the confusion. However, the difference may be explained by fact that the TDR and impulse response of the MIRA were not as good as those of the IRA described above.

The IEEE gain vs. angle off boresight for the defocused mode is given in Figures 8.20 and 8.21 for frequencies from 50 MHz to 2 GHz. The antenna pattern in the H plane, based on the peaks of the raw voltage measurements, is shown in Figure 8.22. The raw data at several angles in the H plane are shown in Figure 8.23. Figures 8.24 and 8.25 provide similar data for the E plane. The half voltage beamwidth is 76° in the H plane and 32° in the E plane. The beamwidth is much wider for the defocused case, which was the reason for building a defocused antenna in the first place. For the half power case, we have beamwidths of 68° and 20° in the H and E planes respectively.

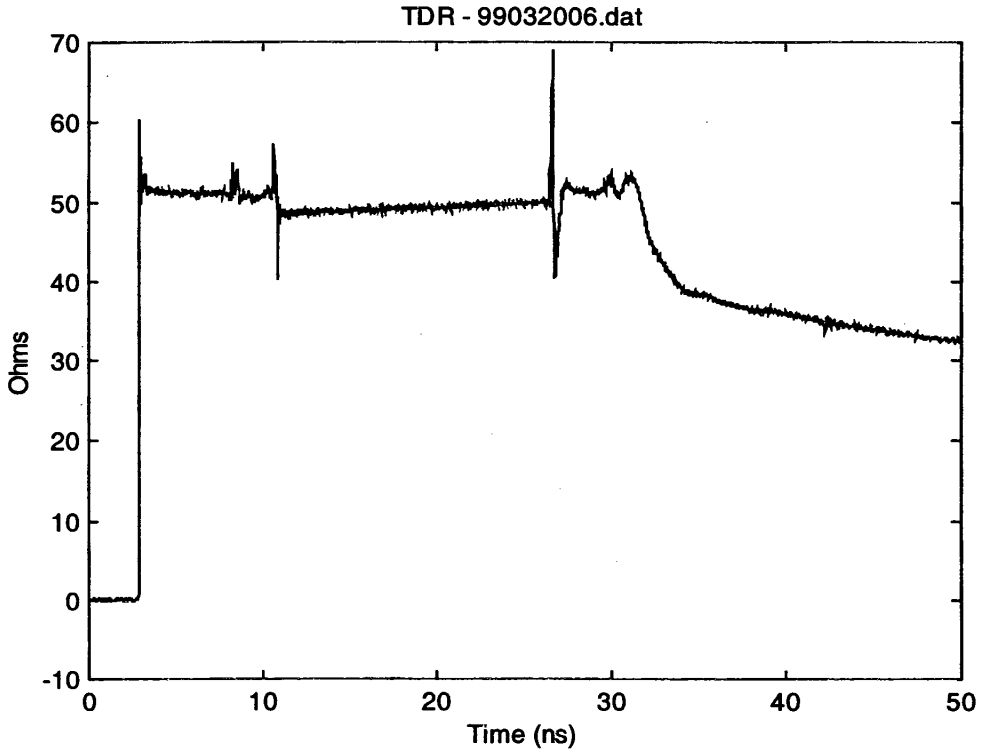

Figure 8.1 TDR of CMIRA with Feed Point Protector (Focused)

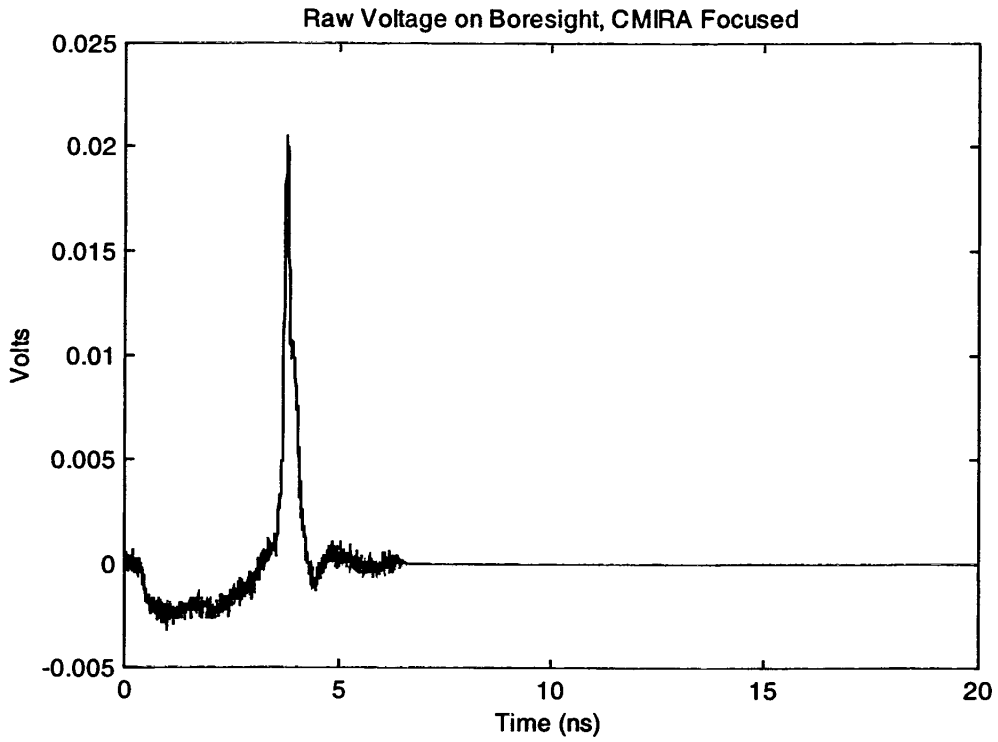

Figure 8.2 Raw Data on Boresight with Ground Bounce Removed and Zero-Padded

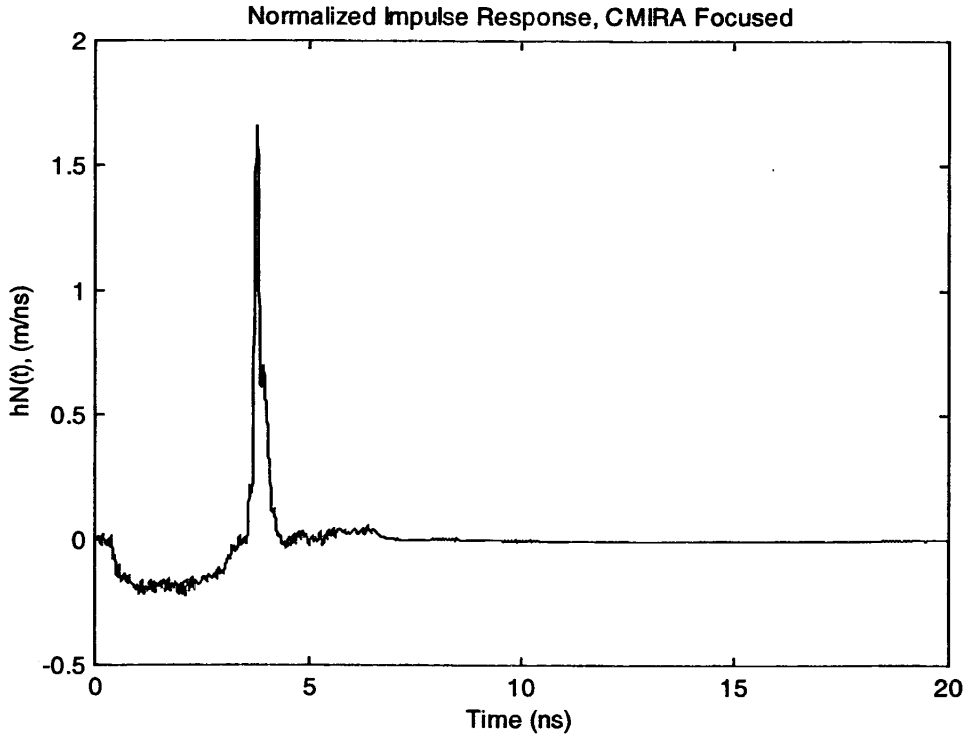

Figure 8.3 Normalized Impulse Response [3]

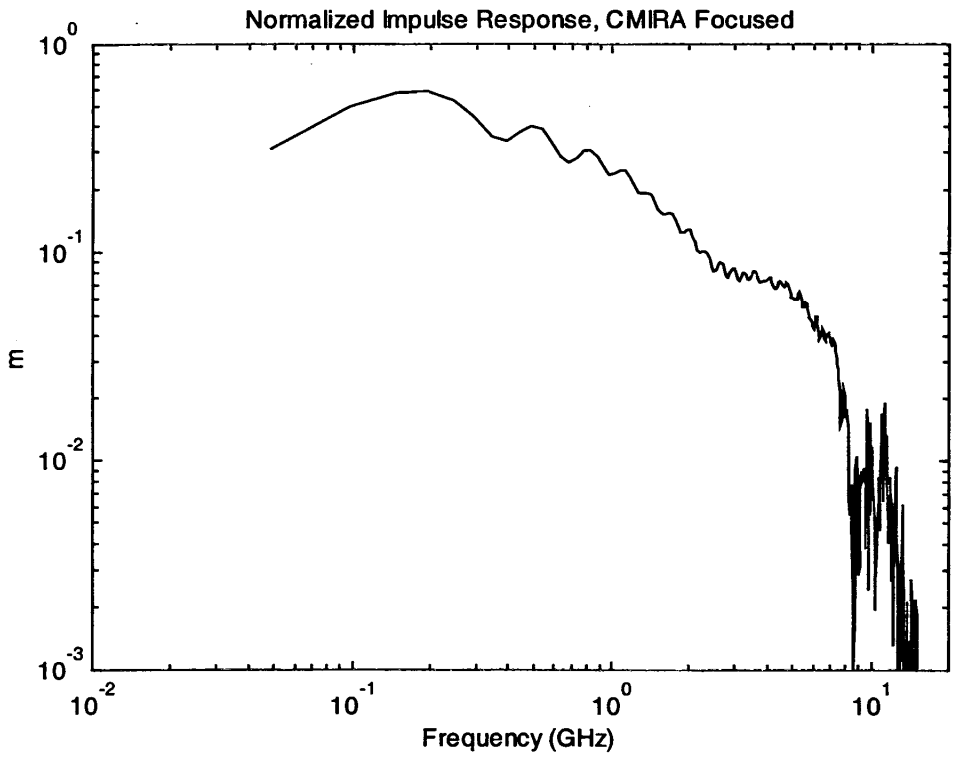

Figure 8.4 Normalized Impulse Response of the CMIRA on Boresight.

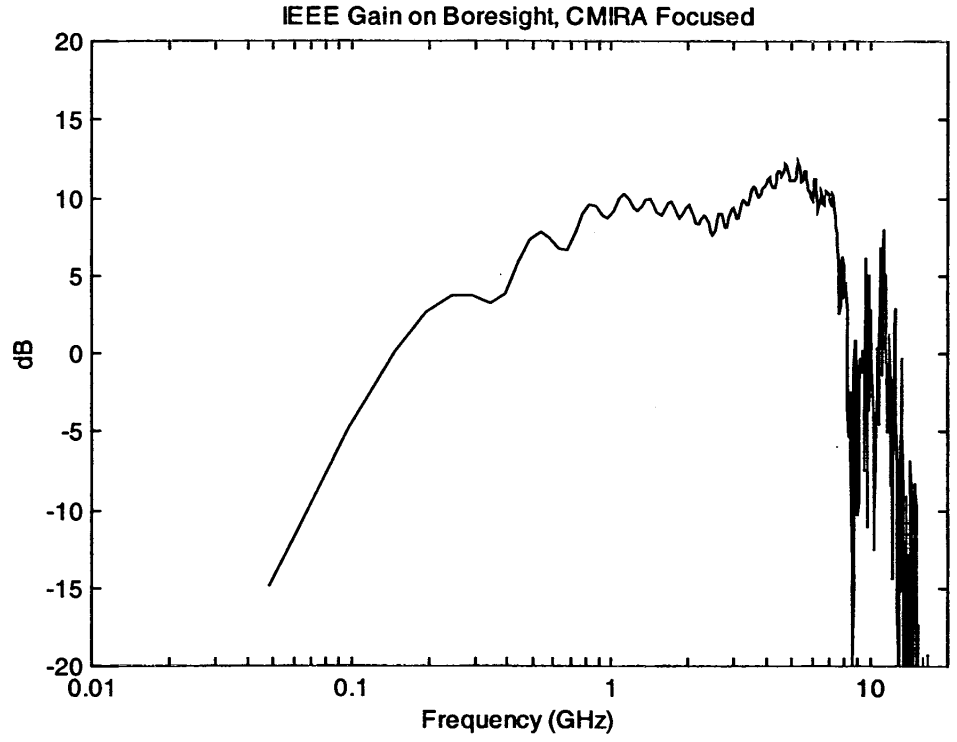

Figure 8.5 IEEE Gain of the CMIRA on Boresight.

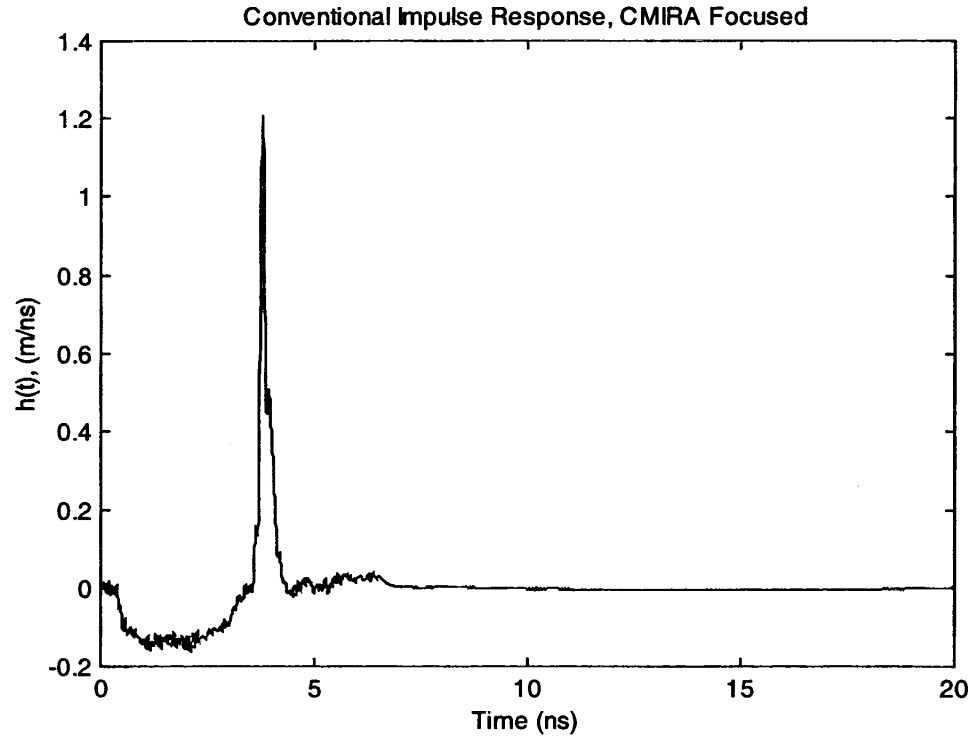

Figure 8.6 Conventional Impulse Response, $h(t)$ [1]

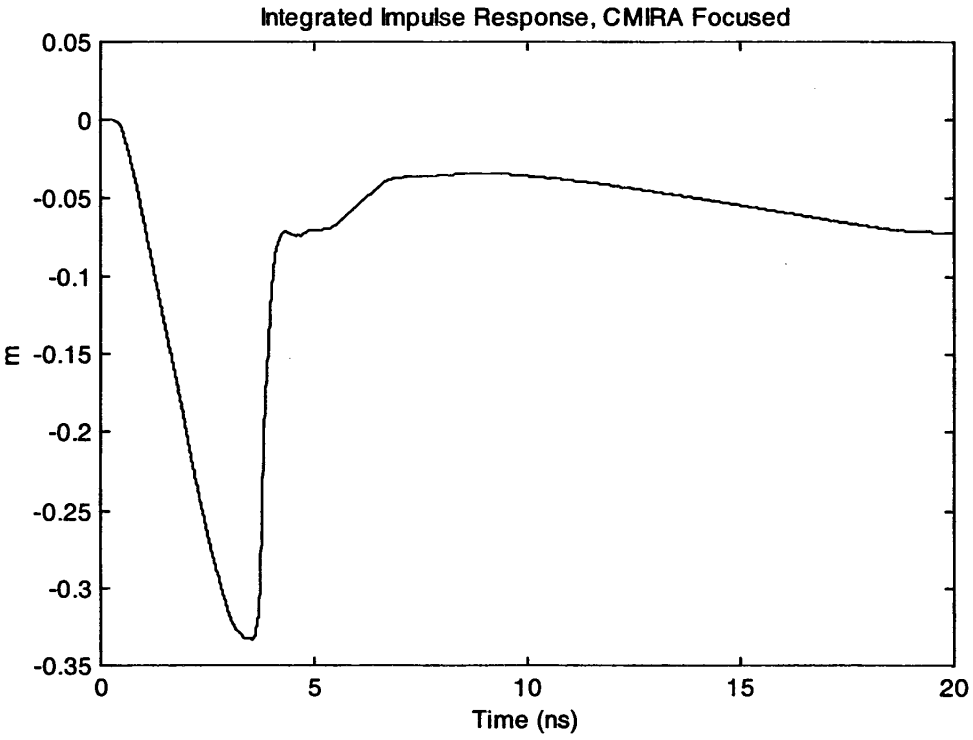

Figure 8.7 Integrated Impulse Response (h_a = 0.26 m, same as CIRA)

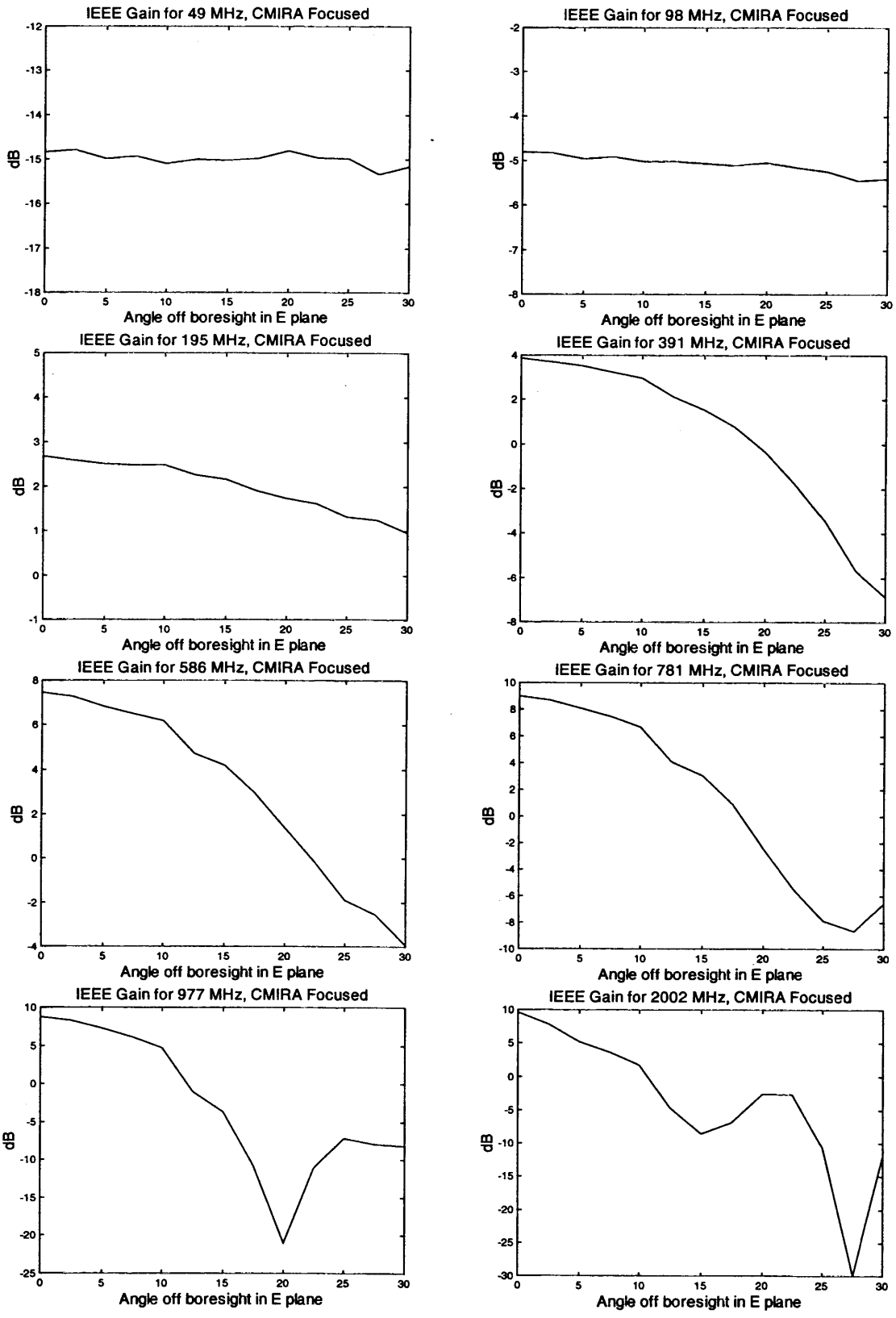

Figure 8.8 IEEE Gain vs. Angle off boresight in E plane

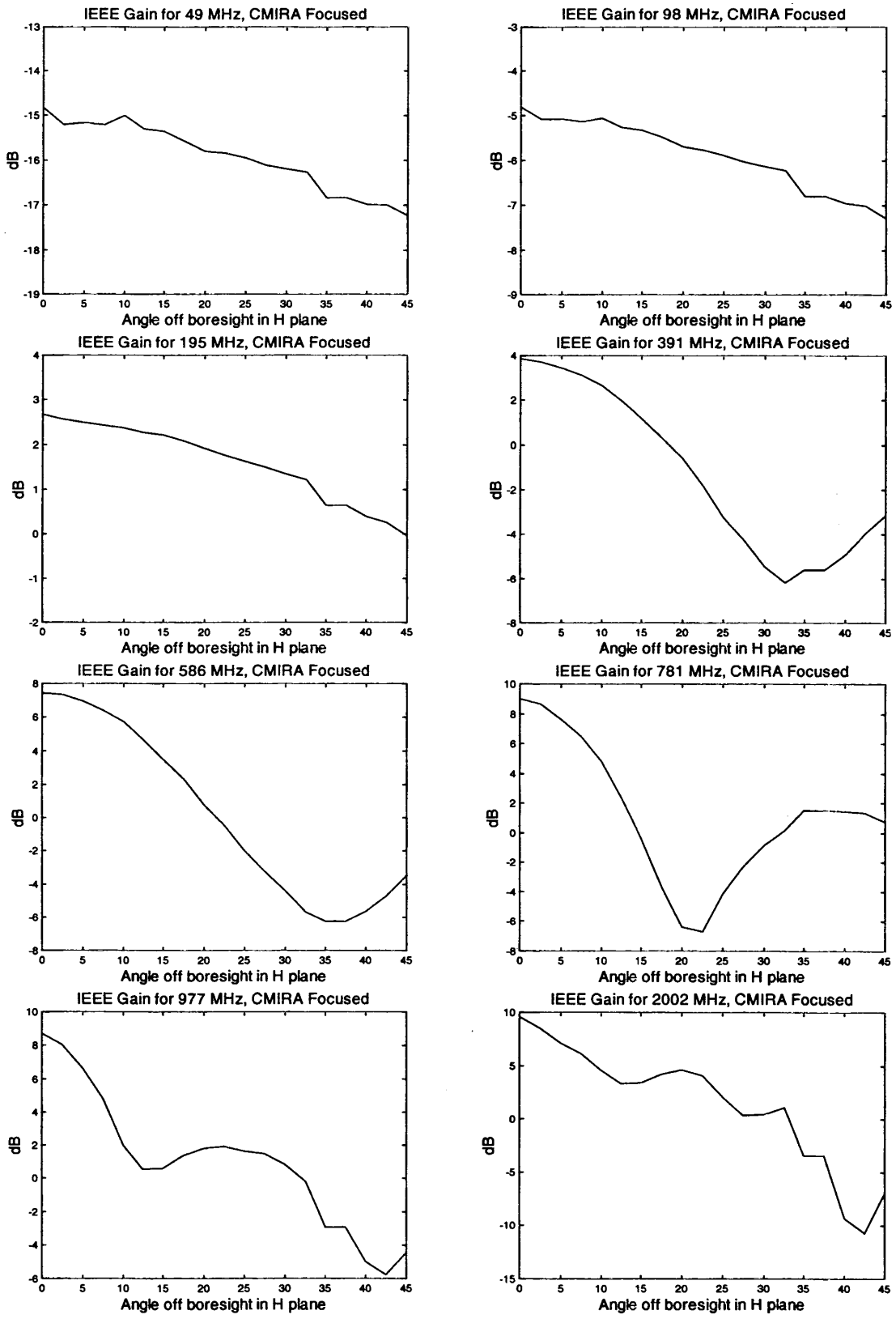

Figure 8.9 IEEE Gain vs. Angle off boresight in H plane

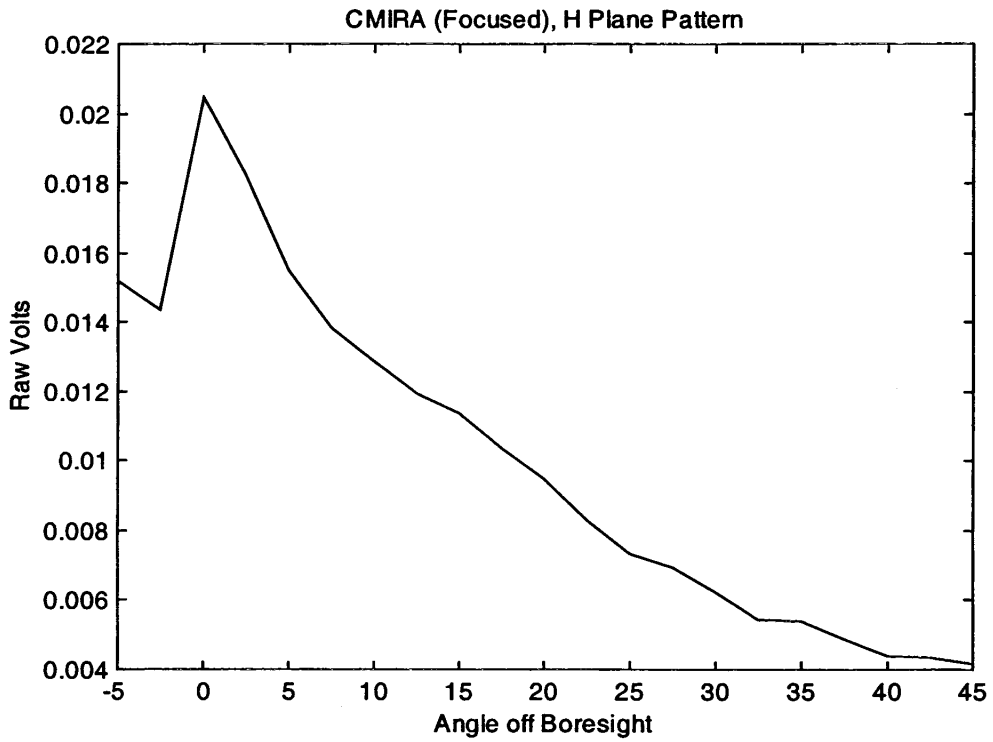

Figure 8.10 Antenna pattern based on raw voltage measurements in H plane.

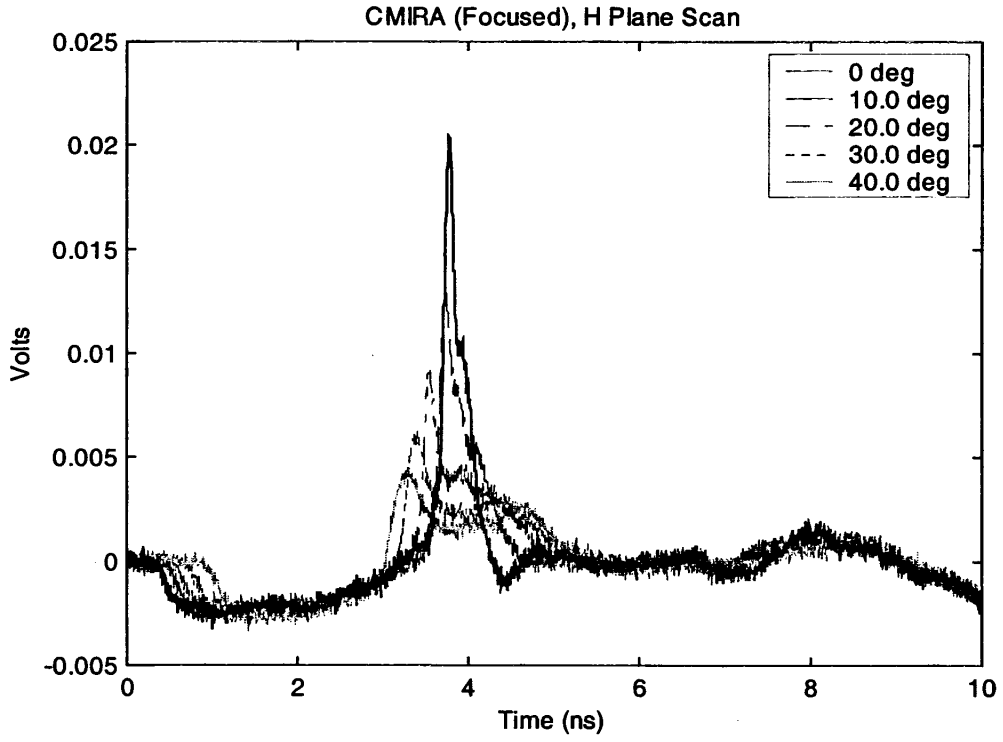

Figure 8.11 Voltage measurements at several angles in H plane.

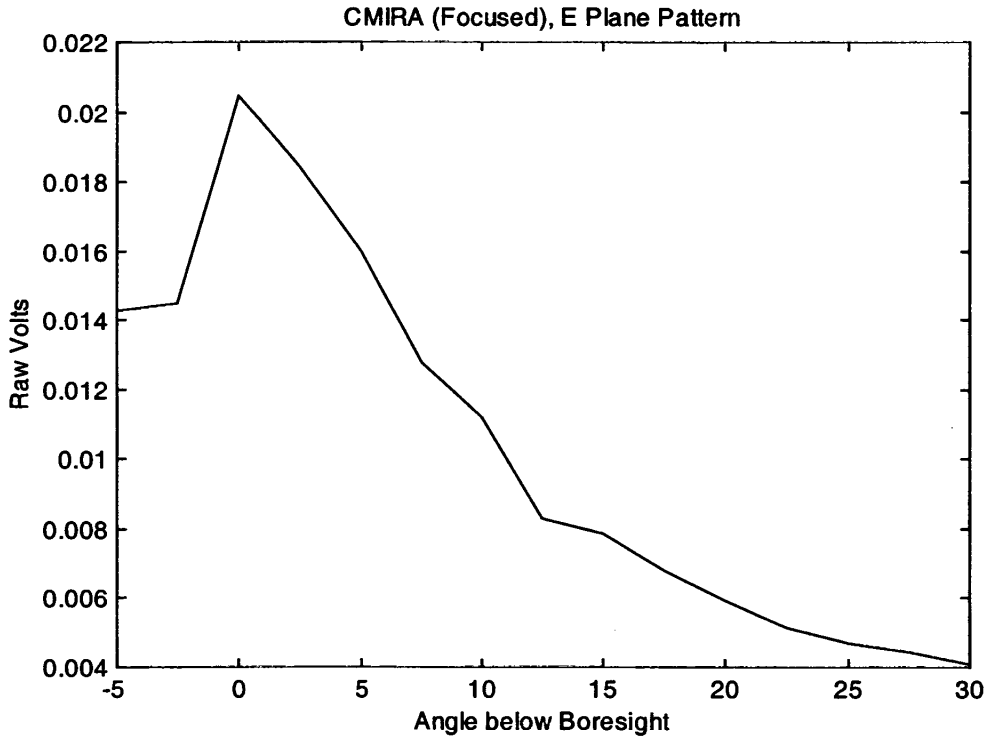

Figure 8.12 Antenna pattern based on raw voltage measurements in E plane.

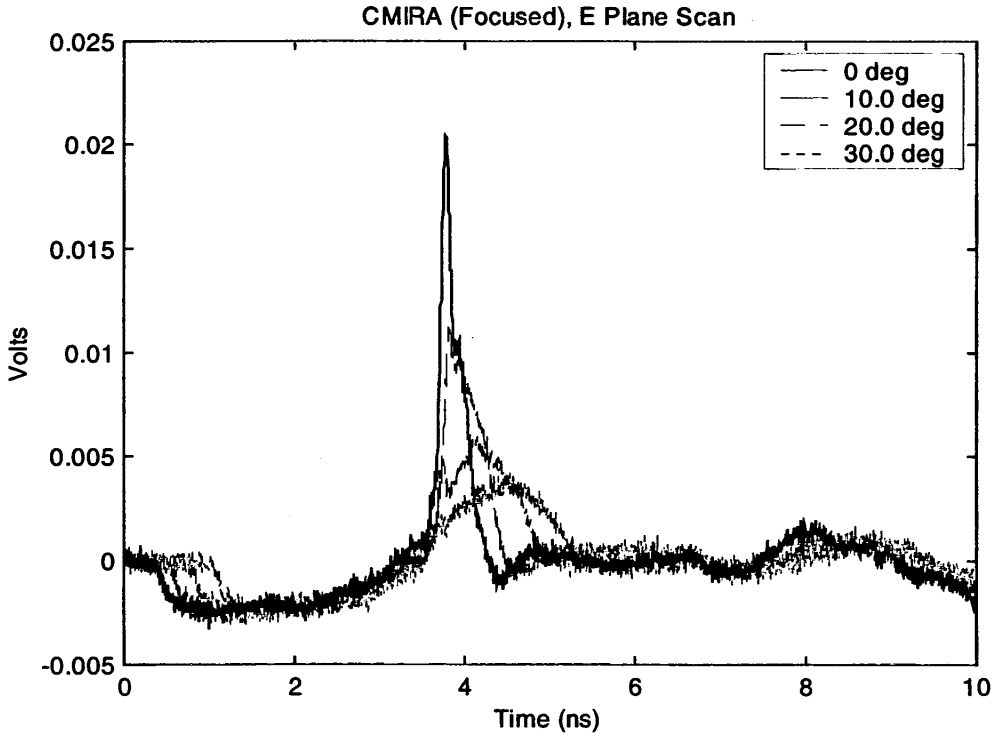

Figure 8.13 Voltage measurements at several angles in E plane.

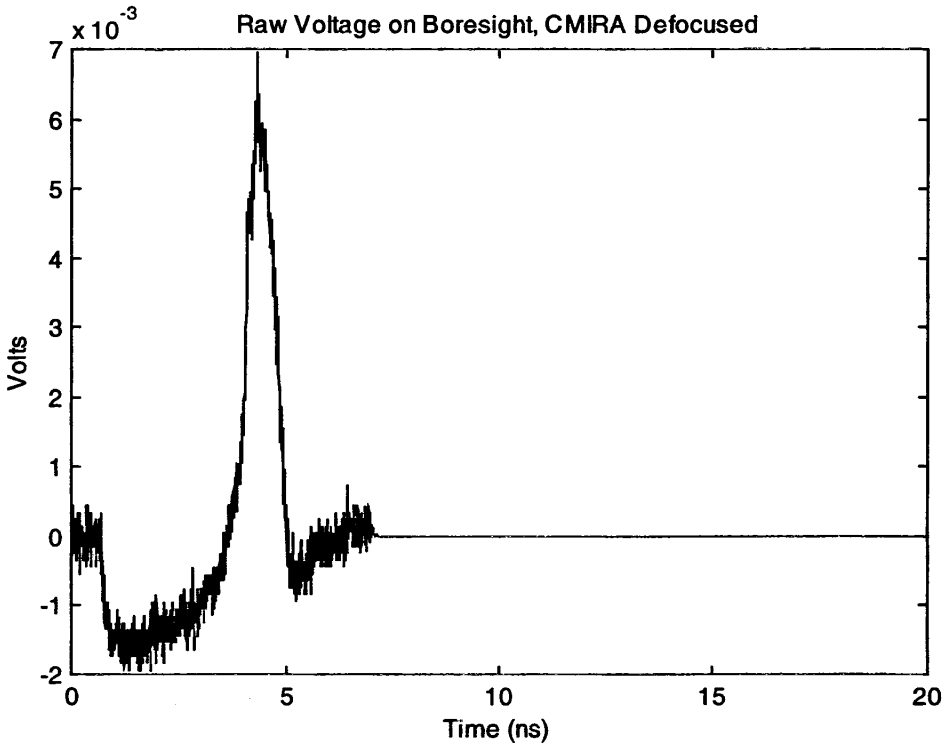

Figure 8.14 Zero-Padded Raw Data on Boresight

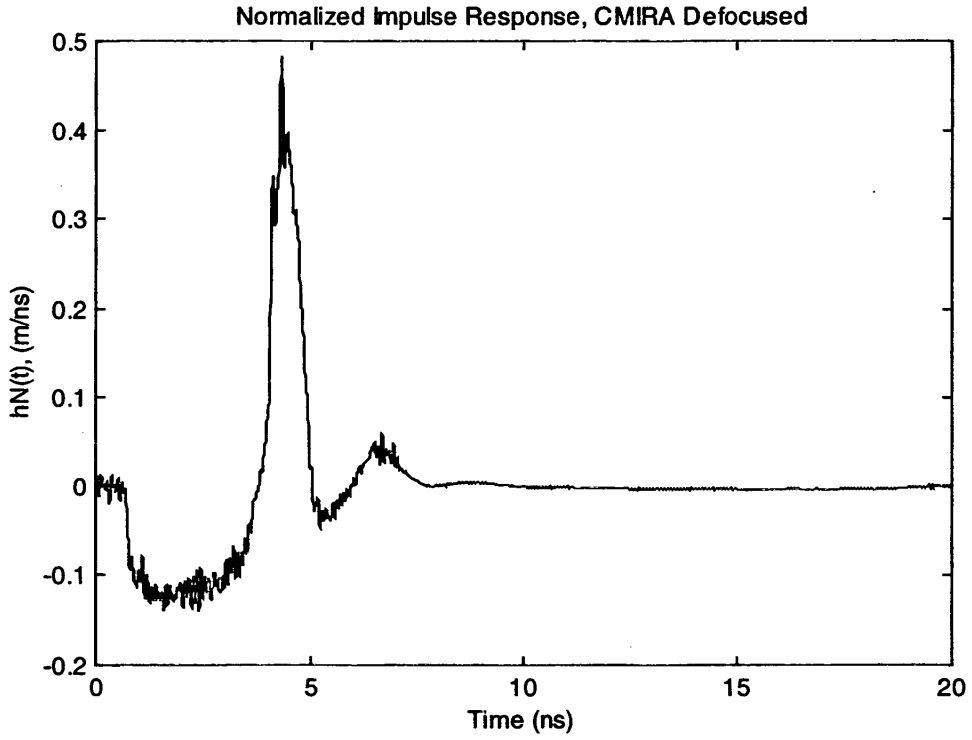

Figure 8.15 Normalized Impulse Response [1]

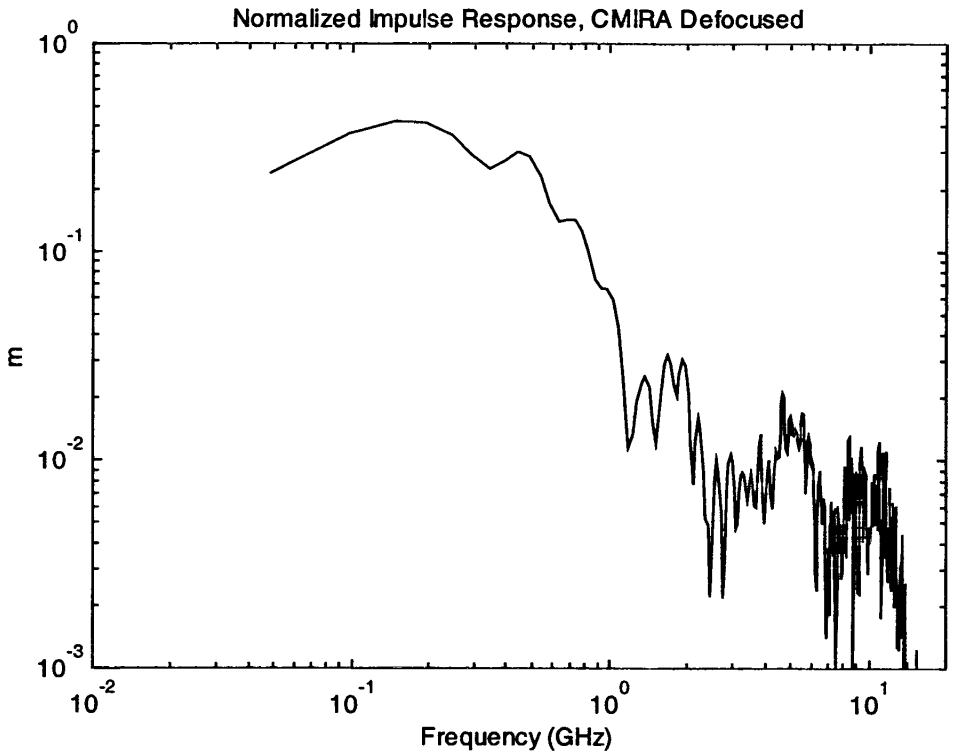

Figure 8.16 Normalized Impulse Response of the CMIRA on Boresight.

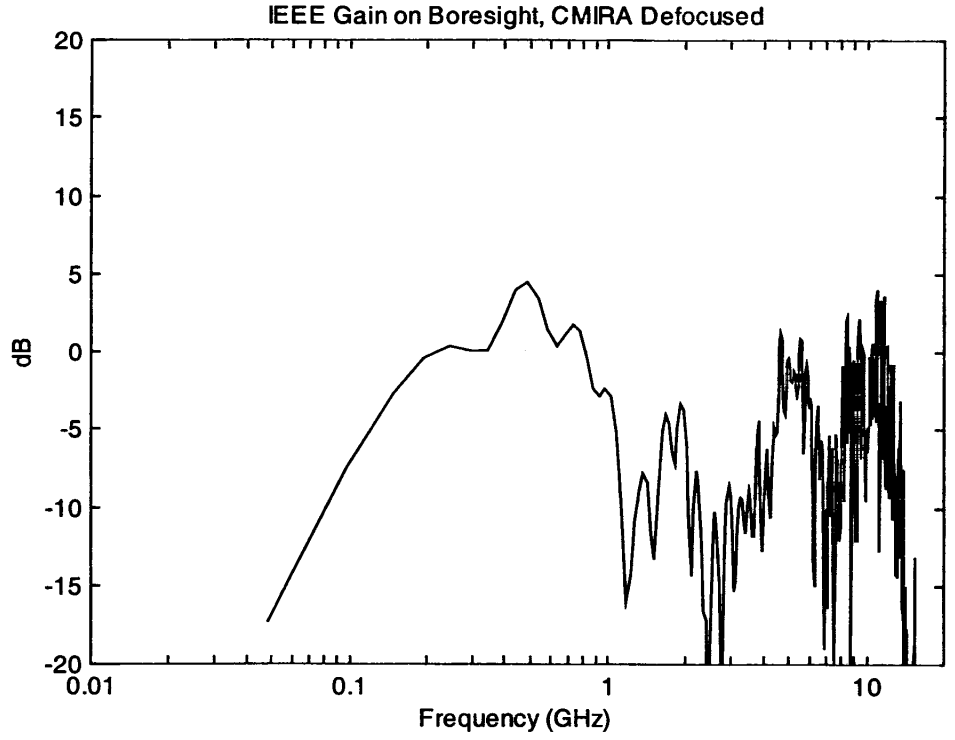

Figure 8.17 IEEE Gain of the CMIRA on Boresight.

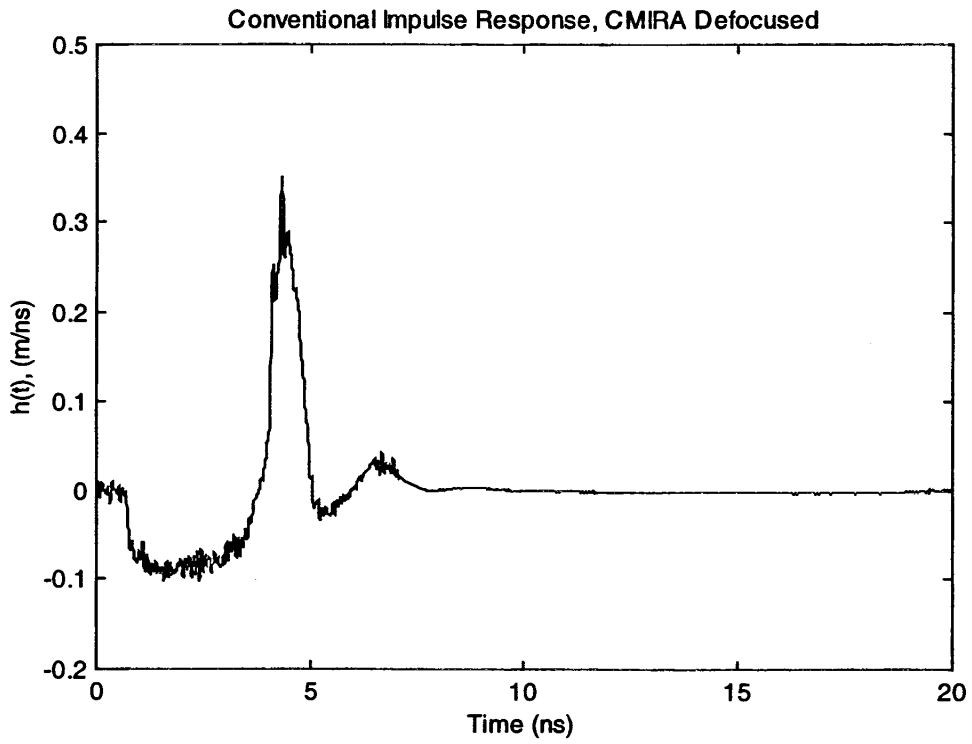

Figure 8.18 Conventional Impulse Response, $h(t)$ [1]

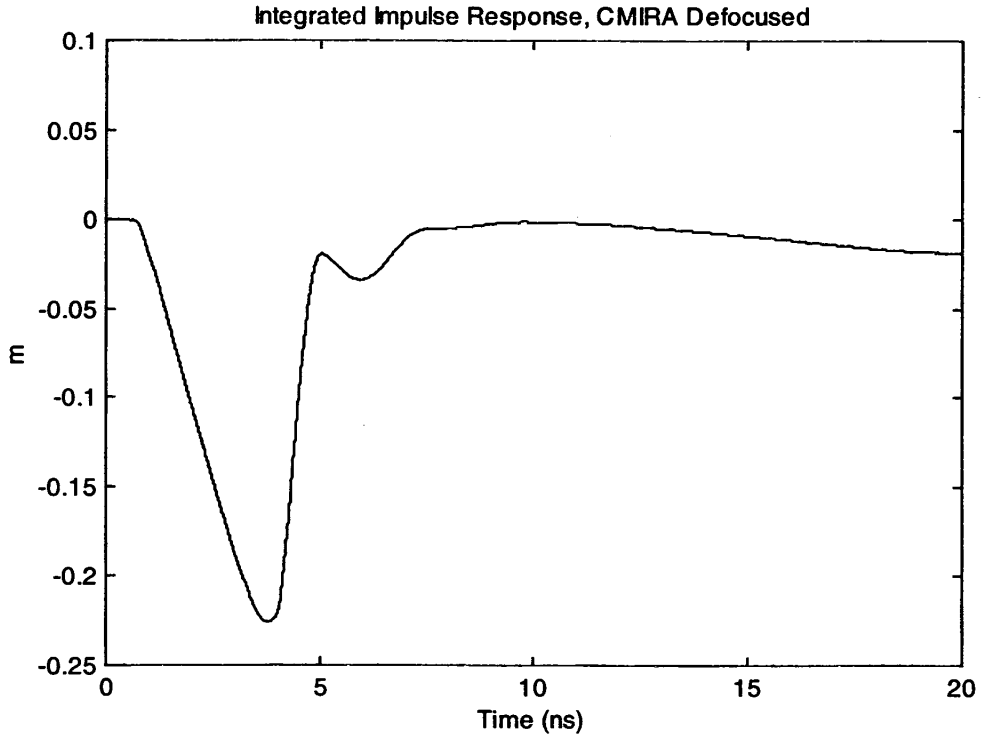

Figure 8.19 Integrated Impulse Response (ha = 0.21 m)

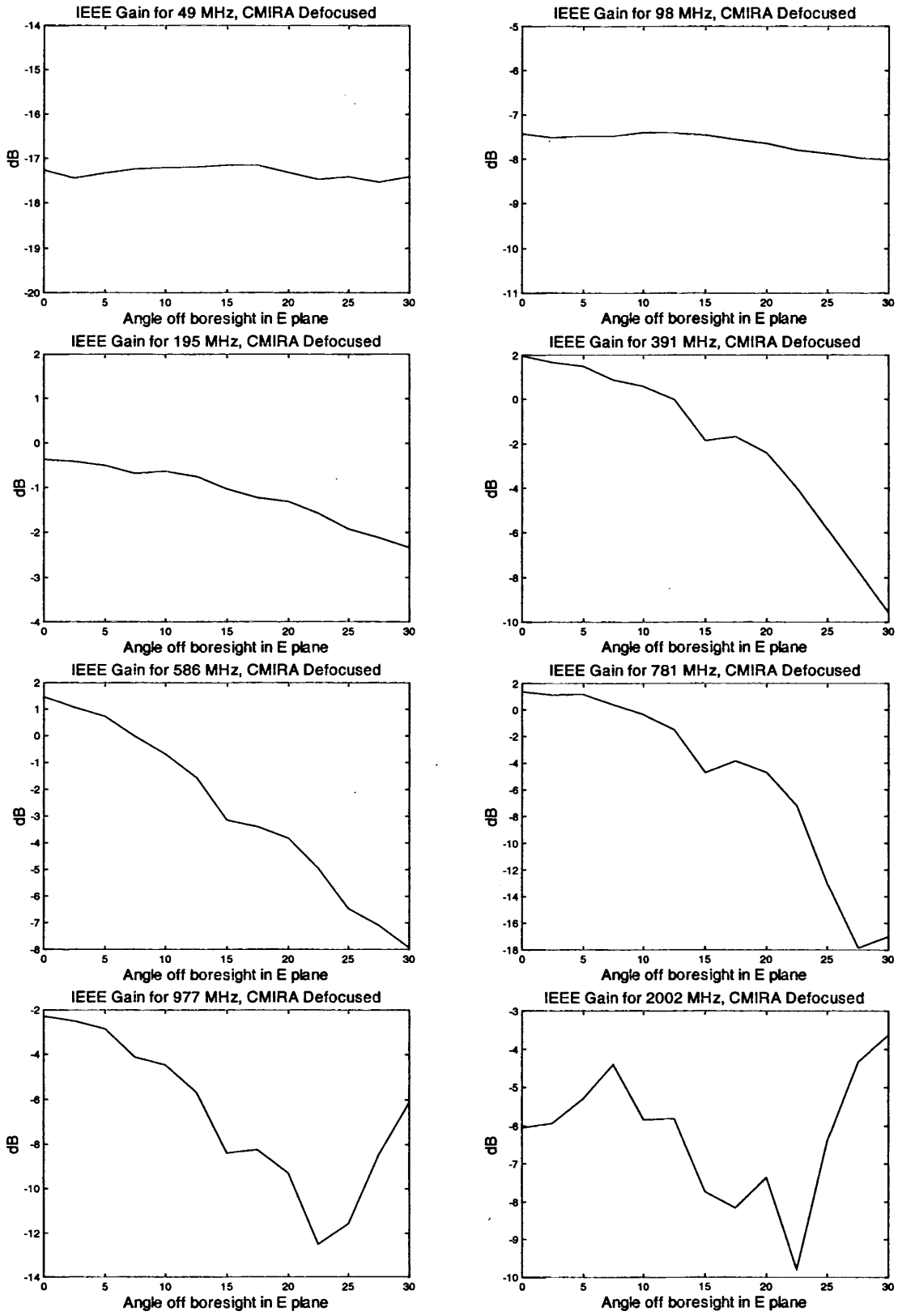

Figure 8.20 IEEE Gain vs. Angle off boresight in E plane

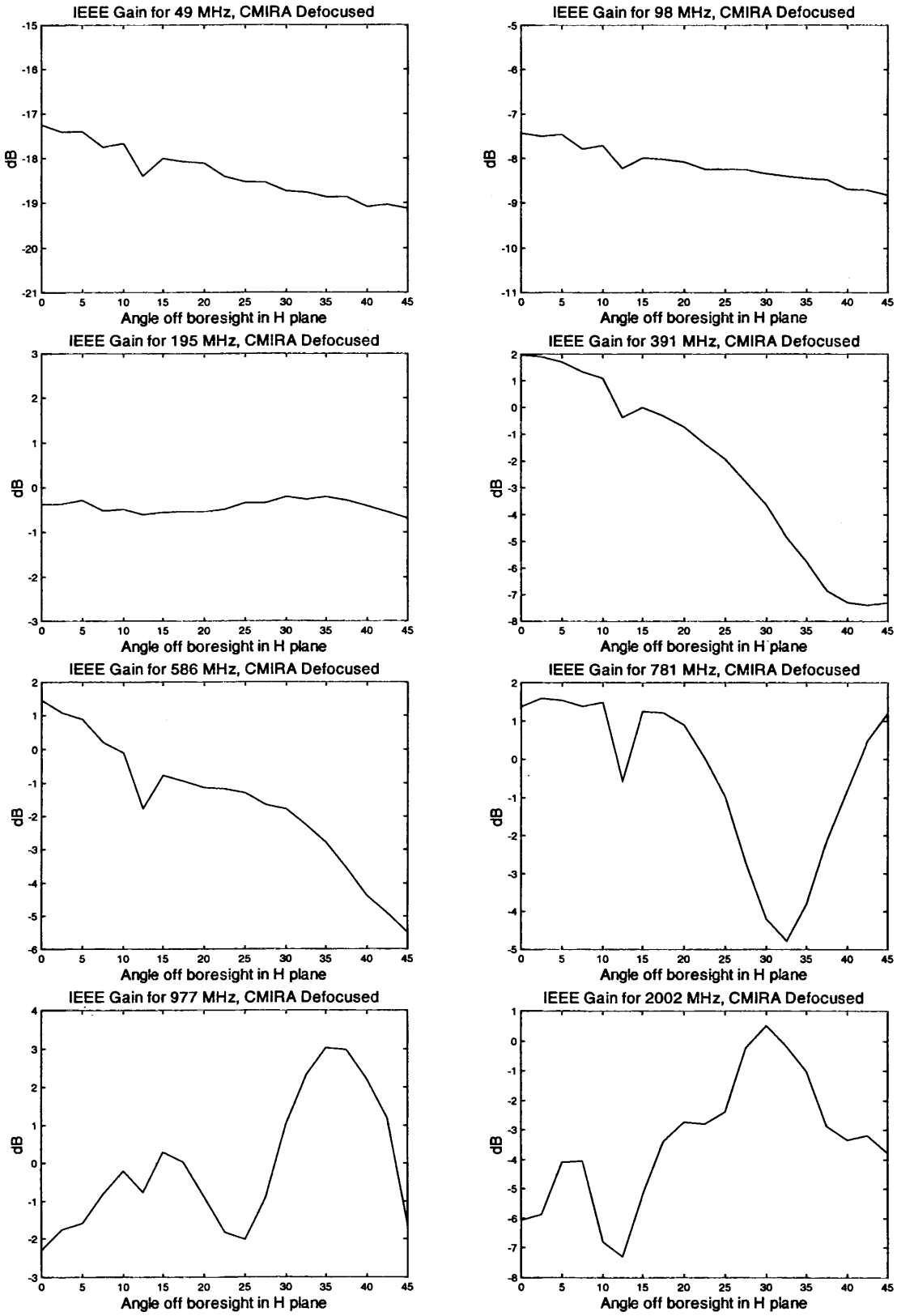

Figure 8.21 IEEE Gain vs. Angle off boresight in H plane

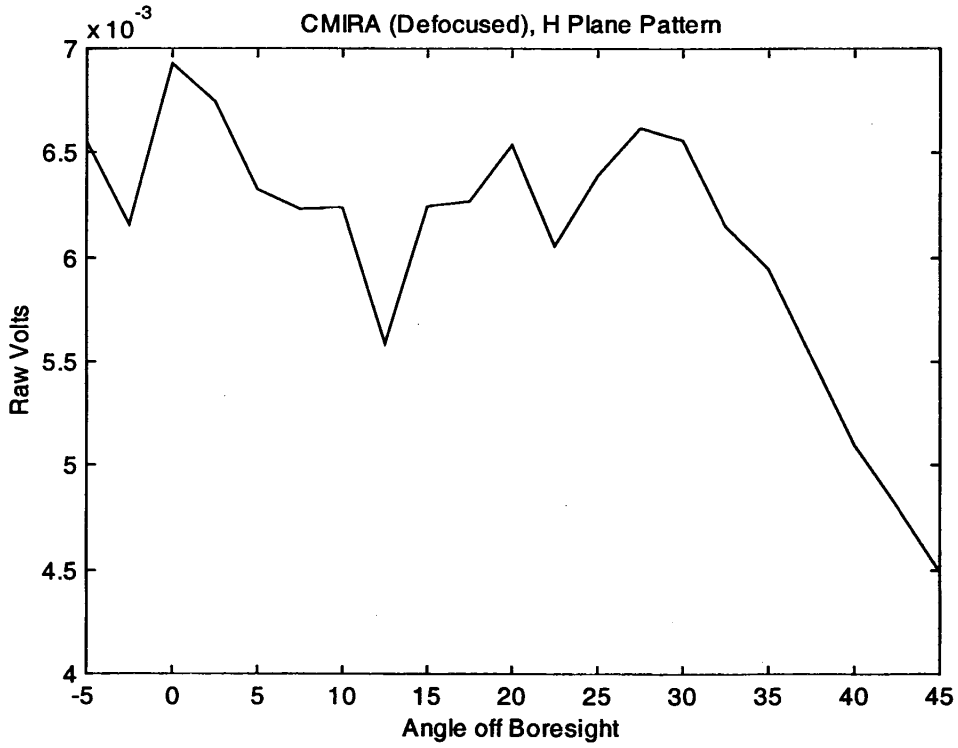

Figure 8.22 Antenna pattern based on raw voltage measurements in H plane.

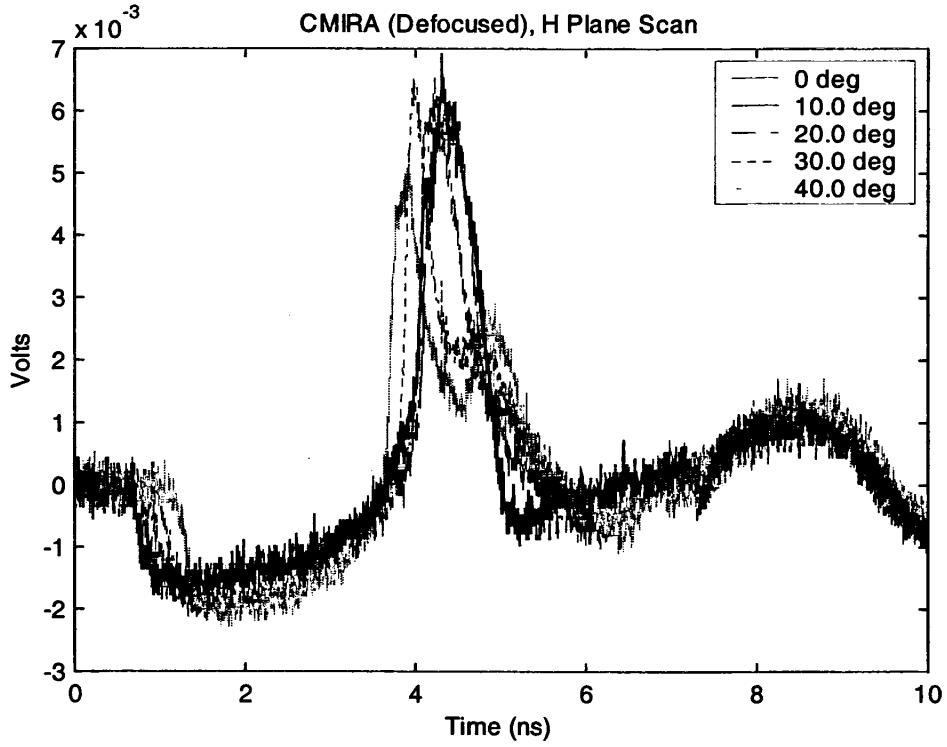

Figure 8.23 Voltage measurements at several angles in H plane.

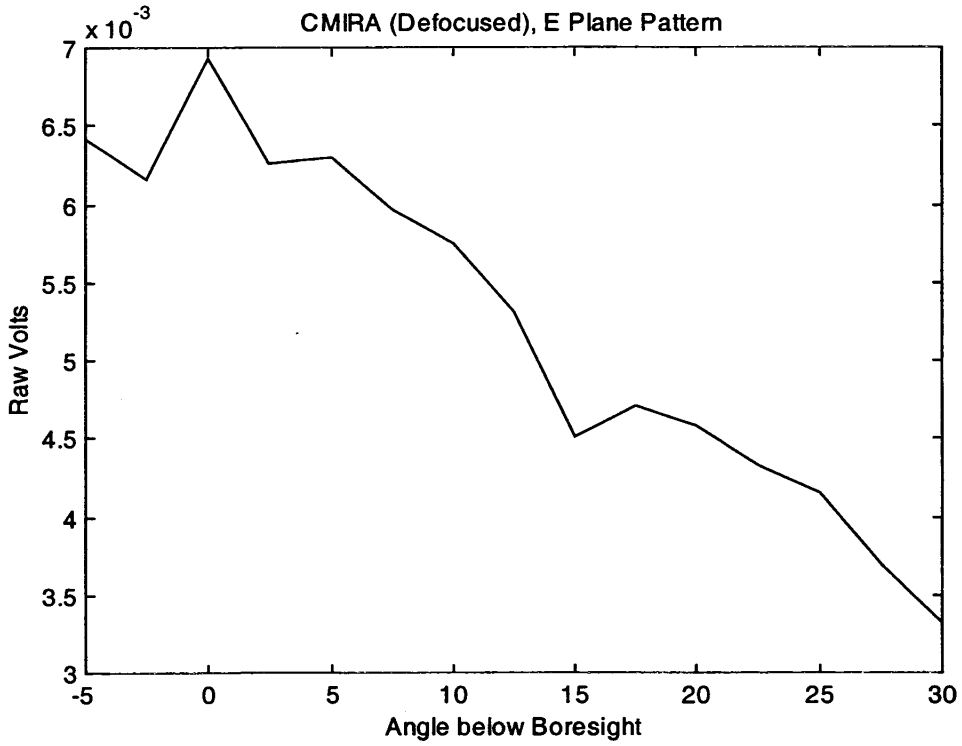

Figure 8.24 Antenna pattern based on raw voltage measurements in E plane.

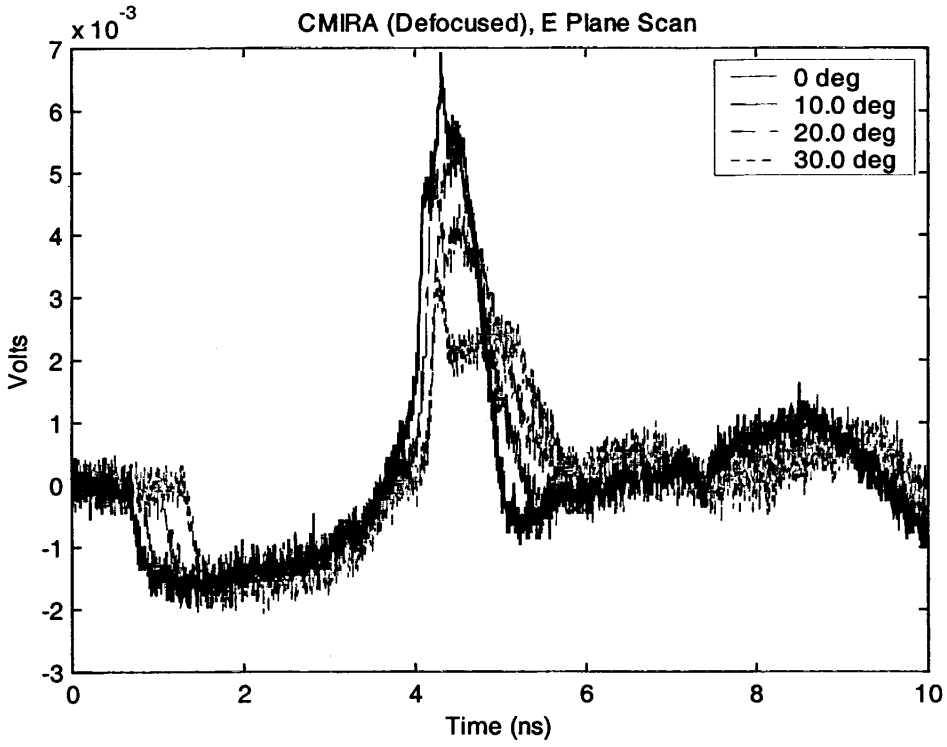

Figure 8.25 Voltage measurements at several angles in E plane.

IX. Conclusions

The design, fabrication, and testing of two first-generation collapsible antennas were described in detail. These antennas met the design requirements for a man portable, 1.22 m (48 in.) diameter MIRA. When folded, the antennas were 127 mm (5 in.) in diameter by 0.736 m (29 in.) long and weight about 2.8 kg (6 lb.). They can be set up in the field by 1-2 people and can be attached to a variety of military and COTS transmitters and receivers.

The antennas utilized an umbrella like design, with a reflector sewn from conductive fabric. This fabric is strong and lightweight but tends to stretch too much and has too much wind resistance. A stronger, open weave fabric has been identified for use on future collapsible antennas.

Although the antennas were reasonably strong, they were both damaged when wind blew over the supporting tripods. The center rods were bent and the unprotected feed point on the CIRA was damaged. Future versions of the CIRA will have a protective cover over the feed point and a stronger center support rod.

The CIRA has a very flat TDR and is usable from below 50 MHz to above 8 GHz. This exceeds the required frequency response of 80 MHz to 2 GHz. The beamwidth in the focused mode is not as narrow as theory predicts. However, this is due to defocusing of the antenna due to stretch in the fabric. The midband effective height of the antenna was within 20% of the theoretical value.

The antennas described here had 20 panels around the circumference of the reflector. It was decided that fewer panels would be sufficient and would reduce weight, size, complexity, and aperture shadowing. Also, fewer stays would require less force to open. The next version of the CIRA will have 12 panels and a closed diameter of about 100 mm (4 in). The new version will also have a stronger center rod and a simpler mechanism for locking the antenna in the open position. Details on the next version will appear in a note to be published shortly.

Acknowledgements

We wish to thank Dr. Carl E. Baum of Air Force Research Laboratory, Directed Energy Directorate, for helpful comments on this work. We also wish to thank Kinetech, Inc., for assistance with the mechanical design.

Patent Notice

A patent is pending on the two antennas described in this note.

References

1. E. G. Farr, C. E. Baum, and W. D. Prather, Multifunction Impulse Radiating Antennas: Theory and Experiment, Sensor and Simulation Note 413, November 1997.

2. L. H. Bowen and E. G. Farr, Recent Enhancements to the Multifunction IRA and TEM Sensors, Sensor and Simulation Note 434, February 1999.

3. E. G. Farr and C. E. Baum, Time Domain Characterization of Antennas with TEM Feeds, Sensor and Simulation Note 426, October 1998.

4. C. E. Baum, E. G. Farr, and C. A. Frost, Transient Gain of Antennas Related to the Traditional Continuous-Wave (CW) Definition of Gain, Sensor and Simulation Note 412, July 1997.

5. E. G. Farr, Optimizing the Feed Impedance of Impulse Radiating Antennas Part 1: Reflector IRAs, Sensor and Simulation Note 354, January 1993.